

# Vertical structure of turbulence and fluxes across cloud mesoscale organizations from the WP-3D Orion aircraft during ATOMIC

Dean Henze<sup>1</sup>, David Noone<sup>2</sup>, Simon De Szoeke<sup>3</sup>, Gijs De Boer<sup>4</sup>, Richard Fiorella<sup>5</sup>, Adriana Bailey<sup>6</sup>, and Peter Blossey<sup>7</sup>

<sup>1</sup>Oregon State University

<sup>2</sup>Waipapa Taumata Rau

<sup>3</sup>Ocean

<sup>4</sup>National Oceanic and Atmospheric Administration

<sup>5</sup>Los Alamos National Laboratory

<sup>6</sup>National Center for Atmospheric Research

<sup>7</sup>University of Washington

January 20, 2023

## Abstract

In-situ measurements of the trade cumulus boundary layer turbulence structure are compared across large-scale circulation conditions and cloud horizontal organizations during the EUREC4A-ATOMIC campaign. The vertical structure of turbulent (e.g. vertical velocity variance, total kinetic energy) and flux (e.g. sensible, latent, and buoyancy) quantities are derived and investigated using the WP-3D aircraft stacked level legs (cloud modules). The 16 cloud modules aboard the P-3 were split into three groups according to cloud top height and column-integrated TKE and vertical velocity variance. These groups map onto qualitative cloud features related to object size and clustering over a scale of 100 km. This grouping also correlates to the large scale forcings of surface windspeed and low-level divergence on the scale of a few hundred km. The ratio cloud top to trade inversion base height is consistent across the groups at around 1.18. The altitude of maximum turbulence is 0.75-0.85 of cloud top height. The consistency of these ratios across the groups may point to the underlying coupling between convection, dissipation, and boundary layer thermodynamic structure. The following picture of turbulence and cloud organization is proposed: (1) light surface winds and turbulence which decreases from the sub-cloud mixed layer (ML) with height generates clouds with generally uniform spacing and smaller features, then (2) as the surface winds increase, convective aggregation occurs, and finally (3), if surface convergence occurs, convection and turbulence reach higher altitudes, producing higher clouds which may precipitate and create cold pools. Observations are compared to a CAM simulation is run over the study period, nudged by ERA5 winds and surface pressure. CAM produces higher column integrated turbulent kinetic energy and larger maximum values on the days where higher cloud tops are observed from the aircraft, which is likely a factor that influences the development of deeper clouds in the model. However, CAM places the peak turbulence 500 m lower than observed, suggesting there may be a bias in CAM representation of turbulence and moisture transport. CAM also does not capture the large LHF's seen for two of the days in which lower cloud tops are observed, which could result in insufficient lower free tropospheric moistening in the model during this type of cloud organization. A large and consistent bias between the model and observations for all cloud groups is the negative SHF's produced in CAM near 1500 m. This is not observed in the measurements. This leads to a net negative buoyancy flux not observed and provides evidence of a specific shortcoming that can be addressed as part of the needed improvement in the representation of clouds by large-scale models.

# Vertical structure of turbulence and fluxes across cloud mesoscale organizations from the WP-3D Orion aircraft during ATOMIC

Dean Henze<sup>1</sup>, David Noone<sup>2</sup>, Simon de Szoeke<sup>1</sup>, Gijs de Boer<sup>3</sup>, Richard Fiorella<sup>4</sup>, Adriana Bailey<sup>5</sup>, Peter Blossey<sup>6</sup>

<sup>1</sup> College of Earth, Ocean, and Atmospheric Sciences, Oregon State University, Corvallis, OR, U.S.A.

<sup>2</sup> Department of Physics, Waipapa Taumata Rau (The University of Auckland), Auckland, New Zealand

<sup>3</sup> Physical Sciences Laboratory, National Oceanic and Atmospheric Administration, Boulder, Colorado, U.S.A.

<sup>4</sup> Computational Earth Sciences Group, Los Alamos National Laboratory, Los Alamos, New Mexico, U.S.A.

<sup>5</sup> National Center for Atmospheric Research, Boulder, CO, U.S.A.

<sup>6</sup> Department of Atmospheric Sciences, University of Washington, Seattle, WA, U.S.A.

*Correspondence to:* Dean Henze (henzede@oregonstate.edu), David Noone (david.noone@auckland.ac.nz)

**Abstract.** In-situ measurements of the trade cumulus boundary layer turbulence structure are compared across large-scale circulation conditions and cloud horizontal organizations during the EUREC4A-ATOMIC campaign. The vertical structure of turbulent (e.g. vertical velocity variance, total kinetic energy) and flux (e.g. sensible, latent, and buoyancy) quantities are derived and investigated using the WP-3D aircraft stacked level legs (cloud modules). The 16 cloud modules aboard the P-3 were split into three groups according to cloud top height and column-integrated TKE and vertical velocity variance. These groups map onto qualitative cloud features related to object size and clustering over a scale of 100 km. This grouping also correlates to the large scale forcings of surface windspeed and low-level divergence on the scale of a few hundred km. The ratio cloud top to trade inversion base height is consistent across the groups at around 1.18. The altitude of maximum turbulence is 0.75-0.85 of cloud top height. The consistency of these ratios across the groups may point to the underlying coupling between convection, dissipation, and boundary layer thermodynamic structure. The following picture of turbulence and cloud organization is proposed: (1) light surface winds and turbulence which decreases from the sub-cloud mixed layer (ML) with height generates clouds with generally uniform spacing and smaller features, then (2) as the surface winds increase, convective aggregation occurs, and finally (3), if surface convergence occurs, convection and turbulence reach higher altitudes, producing higher clouds which may precipitate and create cold pools.

Observations are compared to a CAM simulation is run over the study period, nudged by ERA5 winds and surface pressure. CAM produces higher column integrated turbulent kinetic energy and larger maximum values on the days where higher cloud tops are observed from the aircraft, which is likely a factor that influences the development of deeper clouds in the model. However, CAM places the peak turbulence 500 m lower than observed, suggesting there may be a bias in CAM representation of turbulence and moisture transport. CAM also does not capture the large LHF's seen for two of the days in which lower cloud tops are observed, which could result in insufficient lower free tropospheric moistening in the model during this type of cloud organization. A large and consistent bias between the model and observations for all cloud groups is the negative SHFs produced in CAM near 1500 m. This is not

observed in the measurements. This leads to a net negative buoyancy flux not observed and provides evidence of a specific shortcoming that can be addressed as part of the needed improvement in the representation of clouds by large-scale models.

## 1 Introduction

Trade cumuli are prevalent over the tropics and substantially effect Earth's radiation budget. Their differing response to warming explains a large part of the spread in climate sensitivity across models (Bony and Dufresne 2005; Webb et al. 2006; Medeiros et al. 2008; Vial et al. 2013). Half the spread in climate model sensitivity is thought to be due to differences in water vapor vertical transport tied to convection and large-scale circulations (Sherwood et al. 2014), and therefore understanding these processes and their connection to cloud fraction is important. One aspect of convection that requires further study is the role of cloud mesoscale organization in cloud fraction and vertical moisture transport. For example, recent LES simulations on larger domains show change in cloud fraction due to changes in mesoscale organization (Seifert and Heus 2013; Vogel et al. 2016; Vial et al. 2017). A key challenge is to connect the turbulence and flux profiles to cloud mesoscale organization.

Since shallow cumulus clouds have characteristic sizes smaller than the grid boxes of GCMs, they must be parameterized with sub-grid scale (SGS) schemes. Boundary layer clouds and turbulence have been parameterized using a variety of methods, including higher-order turbulence closure models (e.g. Bougeault 1981a,b; Krueger 1988; Redelsperger and Sommeria 1986), low-order closure models (e.g. Bechtold et al. 1992; Khairoutdinov et al. 2003), and mass flux models (e.g. Arakawa and Schubert 1974). One computationally inexpensive sub-grid scale (SGS) parameterization is the assumed PDF (probability distribution function) higher-order turbulence closure (APHOC) scheme, which e.g. computes moments of liquid water potential temperature  $\theta_l$ , total water  $q$ , and vertical velocity  $w$  to constrain a joint PDF. Once the PDF is known, mass flux, cloud fraction, and higher order turbulent moments can be diagnosed (Golaz et al., 2002; Larson et al. 2002a). The Community Atmospheric Model (CAM) is a GCM implements an APHOC, the Cloud Layers Unified By Binormals (CLUBB, Larson and Golaz, 2005) scheme. However, as discussed elsewhere (Huang et al., 2020), deterioration in CLUBB performance on scales greater than 25 km may be due to mesoscale cloud features. Thus, simultaneous observations of turbulence and flux profiles and horizontal cloud organization are essential to test and improve models. However, full profiles of turbulence and flux quantities in the trade wind region are rare. Previous studies have either focused on the sub-cloud layer (Pond et al., 1971; Lemone and Pennell, 1976; Thompson et al., 1980), entrainment mixing and turbulence on the scale of a single cloud (Starr Malkus, 1954; Katzwinkel et al., 2014; Schmeissner et al., 2015), or LES simulations (Cuijpers et al., 1996; Grant and Lock, 2004). Kollias and Albrecht (2010) provide long term statistics of trade cumulus vertical velocity statistics using radar, but only when and where clouds are present. Full flux profiles were obtained during VOCALs (Dodson and Griswold, 2021) for stratocumulus topped marine boundary layers, but not for trade cumulus boundary layers.

The recent joint field campaigns EUREC<sup>4</sup>A (Elucidating the Role of Cloud-Circulation Coupling in Climate) and ATOMIC (Atlantic Tradewind Ocean-Atmospheric Mesoscale Interaction Campaign) in January and February of 2020 were designed to understand and constrain the connection between large scale circulations, trade-wind cloudiness, and its mesoscale organization (Bony et al., 2017). The campaigns included level leg measurements of 3D wind, temperature, and moisture from the ATR 42 and WP-3D (P-3) Orion aircrafts. The ATR 42 was operated by the French Research Aircraft Infrastructure for Environmental Studies (SAFIRE). The P-3 was operated by the National Oceanic and Atmospheric Administration (NOAA). The results from the ATR 42 have been published as a data paper (Brilouet et al., 2021), but not analyzed in detail. Further, the horizontal, stacked level legs from the P-3 which span the sub-cloud layer, cloud layer, and cloud tops have not yet been analyzed. This study utilizes these measurements and places them in context of cloud mesoscale organization and large-scale forcing (e.g. surface winds, divergence, lower tropospheric stability).

Observations are compared to simulation output from the National Center for Atmospheric Research (NCAR) Community Atmosphere Model version 6 (CAM6) run over the observation period and nudged by horizontal winds and surface pressure from the ERA5 reanalysis. While the limited statistics from the observations makes a robust comparison to the model challenging, the degree to which CAM6 produces turbulence and flux profiles capturing the range of the observations can be tested. This study provides a rare side by side comparison of a GCM to observed turbulence and fluxes. Section 4.3 covers methods, including context for the EUREC<sup>4</sup>A-ATOMIC campaign, relevant measurements and datasets, flux computations, and the means by which P-3 cloud modules are grouped into three categories. Section 4.4 presents results by testing cloud module grouping against large scale forcing quantities derived from reanalysis output, analyzing turbulence and flux profiles from the P-3, and comparing observed profiles to CAM6. A discussion is presented in Section 4.5. Section 4.6 provides final remarks.

## **2 Methods**

### **2.1 EUREC<sup>4</sup>A-ATOMIC study region and data**

The EUREC<sup>4</sup>A-ATOMIC campaign took place in the “Trade Wind Alley” and “Boulevard des Tourbillons” regions of the western Atlantic (Fig. 1). Overviews of the campaign and descriptions of sampling strategies and platforms can be found elsewhere (Bony et al., 2017; Stevens et al., 2021; Pincus et al., 2021). This study focuses on measurements made in the Trade Wind Alley, primarily utilizing the 16 cloud modules performed by the NOAA WP-3D Orion Aircraft “Miss Piggy” (hereafter, P-3) between January 17<sup>th</sup> and February 12<sup>th</sup> (Table 1). The first 11 cloud modules were between noon and 18:00 local time. The last 5 cloud modules occurred at night between 23:00 and 06:00 local time. Cloud modules consisted of 5 stacked levels legs each 12-15 minutes in duration (translating to ~100 km for typical flight speeds of 130 m s<sup>-1</sup>). The altitudes for the five level legs of each cloud module were chosen to target near surface, sub-cloud mixed layer (ML) top, cloud bases, in-cloud, and cloud-tops (Fig. 1).

During level legs, in-situ measurements included air pressure and wind components at 50 Hz, joint water concentration and heavy water isotope ratios at 5 Hz, and static air temperature at 1 Hz. Water vapor and isotope ratio data were collected with a Picarro 2120-i cavity ringdown spectrometer (Bailey et al., 2022), which sampled ambient air through a backwards-facing copper tube, centered within a National Center for Atmospheric Research HIAPER Modular Inlet (HIMIL). Temperature measurements were made with a Rosemount 102AL sensor (Pincus et al., 2021). Processing procedures for the 50 Hz wind measurements is included as an appendix. For each cloud module, 3-5 Vaisala RD41 dropsondes (George et al., 2021) were deployed during the cloud-top leg to obtain vertical profiles of temperature, humidity, and pressure. Estimates of cloud top heights and cloud fractions were obtained from a downward facing W-band (94 GHz) pulsed Doppler radar provided by the NOAA Physical Sciences Laboratory (Moran et al., 2012).

Additional in-situ measurements during EUREC4A/ATOMIC as well as satellite and reanalysis are used to supplement the P-3 cloud module data. Wind / water / temperature measurements from the R/V Ron Brown, deployed within the region for the duration of the experiment, are used to compare sensible and latent heat fluxes to the P-3 near surface measurements. ECMWF ERA5  $0.25^\circ \times 0.25^\circ$  hourly data are used to assess synoptic conditions. GOES-16 2 km resolution infrared brightness temperatures ( $11.2 \mu\text{m}$  channel, Bedka and Palikonda, 2018) were used to assess cloud mesoscale features.

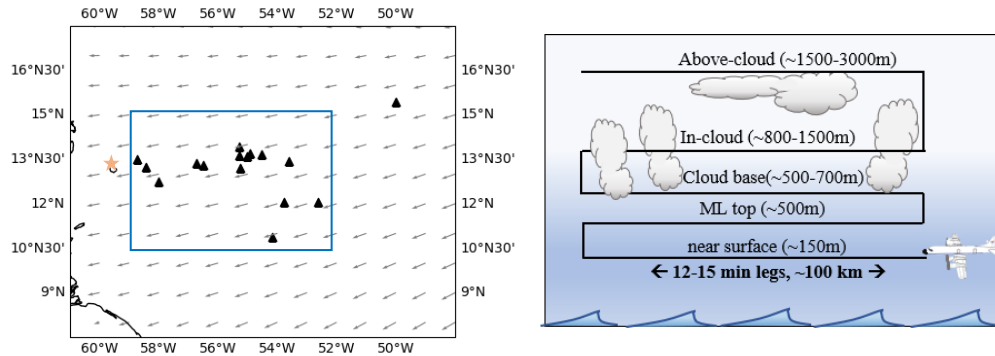


**Figure 1.** (Left) EUREC<sup>4</sup>A-ATOMIC study region (“Trade Wind Alley” in the western Atlantic) with WP-3D aircraft cloud module sampling locations (triangles). Operations were based out of Barbados (red star). The blue box marks the region over which ERA5 synoptic conditions and CAM6 statistics are computed. Mean ERA5 surface winds over the WP-3D OP are shown. (right) Cloud module sampling strategy comprising stacked level legs at targeted altitudes.

## 2.2 Cloud module groups

The 16 cloud modules were split into three groups which ultimately map onto a qualitative metric of cloud mesoscale organization and quantitative cloud top heights as shown in Table 2 and Fig. 2. These groups are referred to here on out as low clouds low turbulence (LCLT), low clouds high turbulence (LCHT), and high clouds high turbulence (HCHT). The original detection of the groups was as follows: the HCHT group was distinguished by

mean cloud top height above 2.5 km as derived from the P-3's W-band radar. The remaining two groups had lower cloud tops and were further distinguished by a clear separation in column integrated  $\overline{w'w'}$  and TKE (see results section). The LCHT group includes profiles with higher values in the vertical region between ML top and trade inversion bottom in all but one case. The exception is a single profile with higher turbulent kinetic energy above the ML, but for which cloud horizontal organization matched better with the LCLT group.

Table 2 shows GOES-16 infrared temperature images during each cloud module. Images are available every 20 minutes and the image with timestamp closest to P-3 mean sampling time is used. The LCLT group shows small cloud features with even spatial distribution. LCHT shows more ‘clustering’ (e.g. larger clouds separated by large areas of clear air). The HCHT group is primarily distinguished by cloud top heights (Fig. 2), but by inspection appears to have broader cloud cover than LCHT and larger cloud features than LCLT. A similar qualitative assessment of cloud mesoscale organization has been done previously for the EUREC4A campaign (Bony et al., 2020; Stevens et al., 2020).

**Table 1.** P-3 cloud module sampling times and locations.

| Cloud Module | Date        | Time          | Lat   | Lon    | Cloud Group |
|--------------|-------------|---------------|-------|--------|-------------|
| 01           | 17 Jan 2020 | 17:17 - 18:46 | 15.4° | -50°   | LCLT        |
| 02           | 24 Jan 2020 | 16:48 - 19:14 | 13.4° | -56.7° | HCHT        |
| 03           | 24 Jan 2020 | 19:14 - 21:14 | 13.3° | -56.5° | HCHT        |
| 04           | 31 Jan 2020 | 19:42 - 21:04 | 13.6° | -55°   | LCLT        |
| 05           | 31 Jan 2020 | 21:12 - 22:33 | 13.6° | -55.3° | LCLT        |
| 06           | 04 Feb 2020 | 15:57 - 17:23 | 13.4° | -53.6° | LCHT        |
| 07           | 04 Feb 2020 | 17:55 - 19:06 | 12.1° | -52.6° | LCHT        |
| 08           | 04 Feb 2020 | 19:36 - 21:12 | 13.2° | -55.3° | LCLT        |
| 09           | 05 Feb 2020 | 16:14 - 17:49 | 12.1° | -53.8° | LCHT        |
| 10           | 05 Feb 2020 | 18:05 - 19:15 | 10.9° | -54.2° | LCHT        |
| 11           | 05 Feb 2020 | 19:29 - 20:55 | 13.7° | -54.5° | LCHT        |
| 12           | 09 Feb 2020 | 02:27 - 03:48 | 13.5° | -58.7° | HCHT        |
| 13           | 09 Feb 2020 | 07:42 - 09:19 | 13.7° | -54.9° | HCHT        |
| 14           | 10 Feb 2020 | 02:07 - 03:50 | 12.8° | -58°   | HCHT        |
| 15           | 10 Feb 2020 | 07:08 - 09:12 | 13.9° | -55.3° | HCHT        |
| 16           | 11 Feb 2020 | 03:36 - 05:01 | 13.3° | -58.4° | HCHT        |

**Table 2.** GOES-16 11.2  $\mu\text{m}$  channel brightness temperatures for each P-3 cloud module, separated into three groups as described in the main text. Overlain in red are flight tracks during cloud module sampling.

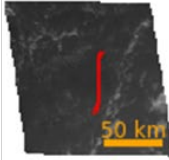
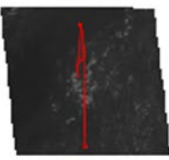
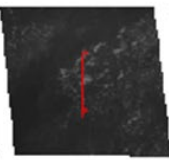
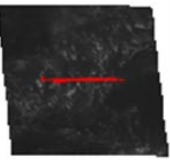
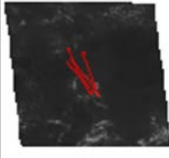
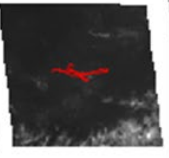
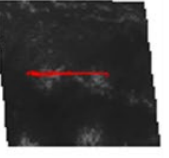
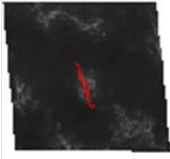
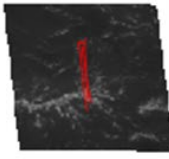
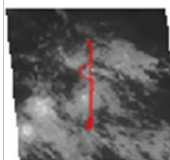
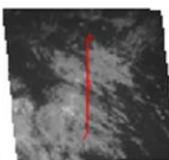
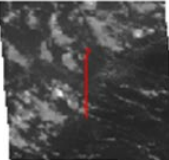
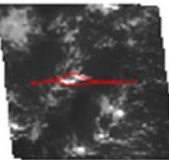
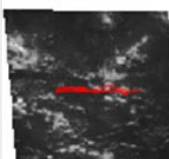
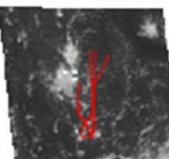
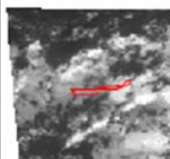
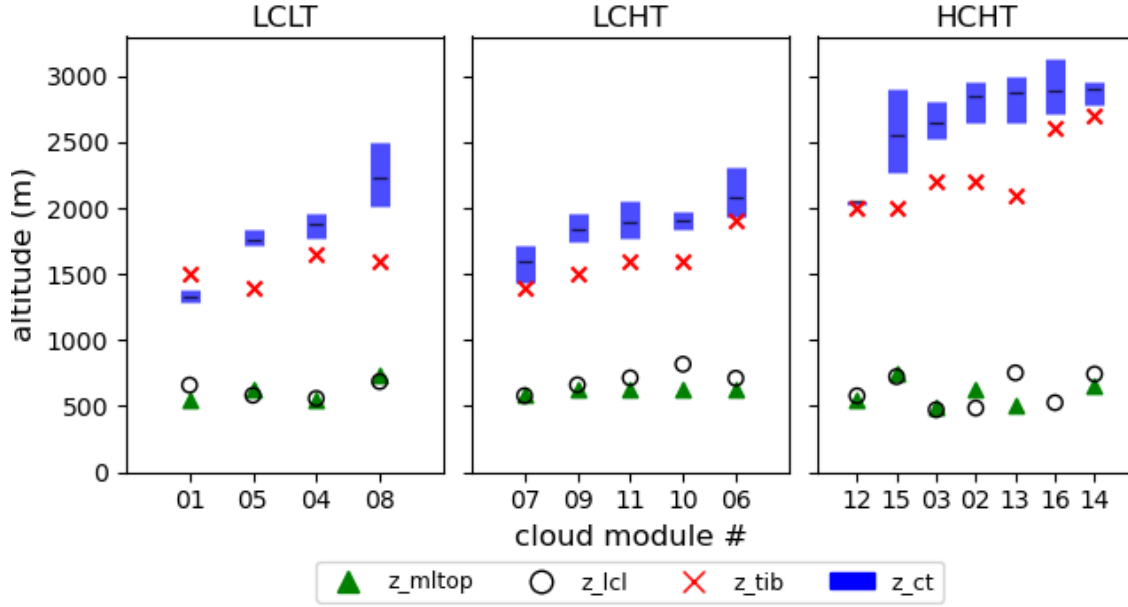
| Cloud group   | P-3 Cloud Modules   |   |  |   |
|---|---|---|--|---|
| LCLT<br>Even distribution of smaller cloud features;<br>Low turbulence  | cld 01<br>   | cld 04<br>   | cld 05<br>   | cld 08<br>   |
| LCHT<br>Cloud clustering (cloud-free regions present);<br>High turbulence between ML top and trade inversion base | cld 06<br>   | cld 07<br>   | cld 09<br>   | cld 10<br>    |
|   | cld 11<br> |   |  |   |
| HCHT<br>Highest cloud tops (> 2.5 km);<br>High turbulence between ML top and trade inversion base                 | cld 02<br> | cld 03<br> | cld 12<br> | cld 13<br> |
|   | cld 14<br> | cld 15<br> | cld 16<br> |   |

Figure 2 summarizes characteristic altitudes associated with trade cumulus marine boundary layer structure, specifically sub-cloud mixed layer (ML) top, lifting condensation level (LCL), trade inversion bottom (TIB), and cloud top (CT). Mixed layer tops are defined as the altitude at which potential temperature  $\theta$  increases by 0.25 K of

its 100 – 300 m mean as determined from dropsondes. LCL is computed from surface values of  $q$ ,  $T$ ,  $P$  from the dropsondes using the equation in Bolton (1980). Trade inversion bottoms are identified as the altitude at which temperature lapse rates become more stable than moist adiabatic for at least 200 m above. P-3 W-band radar is used to obtain the 50<sup>th</sup>-95<sup>th</sup> percentile range of detected cloud tops during the cloud-top leg of each cloud module. The 50<sup>th</sup> percentile was used as a lower cutoff to avoid artifacts from radar detection of the sides of clouds.



**Figure 2.** LCL, mixed layer depth, and trade inversion base computed from dropsondes for each cloud module, separated into groups as defined in Table 2 and ordered by cloud top height within each group. Blue bars are the range of cloud tops from 50<sup>th</sup> to 95<sup>th</sup> percentiles during the above cloud leg from the downward facing radar, with black lines showing the mean of data in the 50<sup>th</sup>-95<sup>th</sup> percentile.

### 2.3 Turbulence and flux calculations

Water mixing ratio and isotope data were synchronized to the aircraft clock (see Henze et al 2022), which ensures alignment with wind fluctuations. After time correction, total kinetic energy (TKE) and the horizontal component of TKE of each level leg were computed as

$$TKE = \frac{1}{2} (\overline{u'^2} + \overline{v'^2} + \overline{w'^2}), \quad (1a)$$

$$TKE_h = \frac{1}{2} (\overline{u'^2} + \overline{v'^2}), \quad (1b)$$



where  $u'$ ,  $v'$ , and  $w'$  are the fluctuations of the velocity components in normal earth coordinates (primes indicate deviations from the horizontal leg means). Sensible heat flux, latent heat flux, and buoyancy flux were computed respectively as:

$$F_{sh} = C_p \bar{\rho} \overline{w' \theta'}, \quad (2)$$

$$F_{lh} = L_v \bar{\rho} \overline{w' q'}, \quad (3)$$

$$F_b = g \frac{\overline{w' \theta_v'}}{\bar{\theta}_v} \quad (4)$$

where  $C_p$  is the specific heat of air ( $1005 \text{ J kg}^{-1} \text{ K}^{-1}$ ),  $L_v$  is the latent heat of vaporization at  $20^\circ\text{C}$  ( $2.45 \times 10^6 \text{ J kg}^{-1}$ ),  $\bar{\rho}$  is the mean air density, and  $\theta'$ ,  $q'$ , and  $\theta_v'$  (given by  $\theta_v = \theta(1 + 0.61q)$ ) are the potential temperature, mixing ratio, and virtual potential temperature perturbations, respectively. Overbars indicate a time average. The time mean of covariant quantities were computed from the cospectra (e.g. Sørensen and Larsen, 2010) after a 1 minute ( $\sim 8 \text{ km}$ ) high pass filter was applied. Cospectra were estimated for each level leg using the mean of 4-6 spectra derived from Hamming windows with a 4-minute bandwidth and linear detrending. Data where aircraft roll was greater than  $5^\circ$  were imputed with the leg-mean value ( $\sim 0$  for perturbation quantities). The robustness of bandpass filter cutoff and window size are discussed below.

Figure 3 shows frequency-weighted power spectra for  $w'$ ,  $\theta'$ ,  $q'$  and  $q_D'$  (HDO mixing ratio) for three legs of cloud module 04. Higher frequencies following a slope of  $f^{-2/3}$  suggests the data sample isotropic turbulence and there is not significant loss of flux at higher frequencies. The roll off of  $q'$  and  $q_D'$  at 1 Hz and above is also seen in Fig. 1 of Dodson and Griswold (2021) even when using 40 Hz data, suggesting either that the limitations of a 5 Hz measurement is modest or that the inlets used in both studies limit the measurement response to 1 Hz. The lowest frequency resolved, having a period of 2 minutes, corresponds to eddies with a spatial scale of approximately 15 km with a typical airspeed of  $130 \text{ m s}^{-1}$ , while the highest frequency resolved, 0.4 seconds, corresponds to eddies with a length scale of approximately 50 m. Maximum variability occurs for 0.1 – 0.3 Hz (1.3 – 4 km) which is also the case for covariances. For wind measurements, the 10 Hz data were also tested to see if there is significant loss of information from using 5 Hz data. Differences were less than 5 %, supporting the use of the 5 Hz data. P-3 derived fluxes from this study are within the range of those from the ATR 42 data product (Brilouet et al., 2021) providing validation. The P-3  $\overline{w'w'}$ , TKE, and  $\overline{w'q'}$  measurements tend toward the higher end of the ATR range. This could be the result of the P-3 targeting cloudy boundary layers, while the ATR had a fixed sampling location and presumably the resulting dataset includes cases of cloud-free MBLs with lower convective activity.

Appropriate windowing and bandpass filtering are key components of eddy covariance computations (e.g. Lenschow et al. 1994). Most studies focus on the sub-cloud layer, where isotropic turbulence is expected to dominate and characteristics are better understood. In the trade cumulus region and free troposphere, the dominant length scales require further assessment. As a guide to understand how the flux computations vary with window length scale (e.g.

if mesoscale and larger features contribute to the computed flux), fluxes for each level leg were recomputed with windows between 30 s (~4 km) and 5 minutes (~40 km). The fractional change in computed flux  $F$  from some reference window is defined as:

$$f_{W0}(W, F) = (F_W - F_{W0})/F_{W0} , \quad (5)$$

Where  $F_W$  is the computed covariance flux for window length  $W$  and  $W0$  is the reference window length. Figure 4 shows that as  $W$  increases from 30 s to 75 s, the covariance  $\overline{w'q'}$  increases by 30 %, but changes negligibly afterwards. We choose a 4-minute window (~30 km) matching Brilouet et al. (2021). Additionally a high band pass filter is applied with cutoff frequency corresponding to a period of 60 s (~15 km), almost 2 x theirs in order to capture potentially larger features from mesoscale organization. It is noted that shortening the window size even in the range 30 s to 2 minutes did not change the results qualitatively, only quantitatively.

## 2.4 isoCAM simulation

The EUREC4A observation period was simulated using the National Center for Atmospheric Research (NCAR) Community Earth System Model (CESM) version 2 (Danabasoglu et al., 2020). The Community Atmosphere Model version 6 (CAM6) was setup to incorporate water isotope ratio tracers (Fiorella et al., 2021; Nusbaumer et al., 2017). The atmospheric grid was  $0.9 \times 1.25^\circ$  horizontal resolution with 30 vertical hybrid layers extending from the surface to ~3 hPa and used the finite volume dynamical core. The dynamics of the CESM simulation was constrained to match the ERA5 reanalysis dataset (Hersbach et al., 2020) by applying a nudging tendency to horizontal winds and surface pressure at each time step. This effectively nudges the divergence as well. The strength of the nudging tendency ( $F_{nudge}$ ) is determined by both the difference between the atmospheric state in ERA5 ( $S_{ERA5}$ ) and CAM6 ( $S_{CAM6}$ ), as well as the difference in time between the current CAM6 model time and the next analysis state of ERA5 ( $\Delta t_{nudge}$ ):

$$F_{nudge} = \frac{S_{ERA5} - S_{CAM6}}{\Delta t_{nudge}} , \quad (6)$$

Other boundary conditions for the model, including sea-surface temperatures, sea-ice and aerosol distributions, and CO<sub>2</sub> concentrations, were prescribed based on historical values.

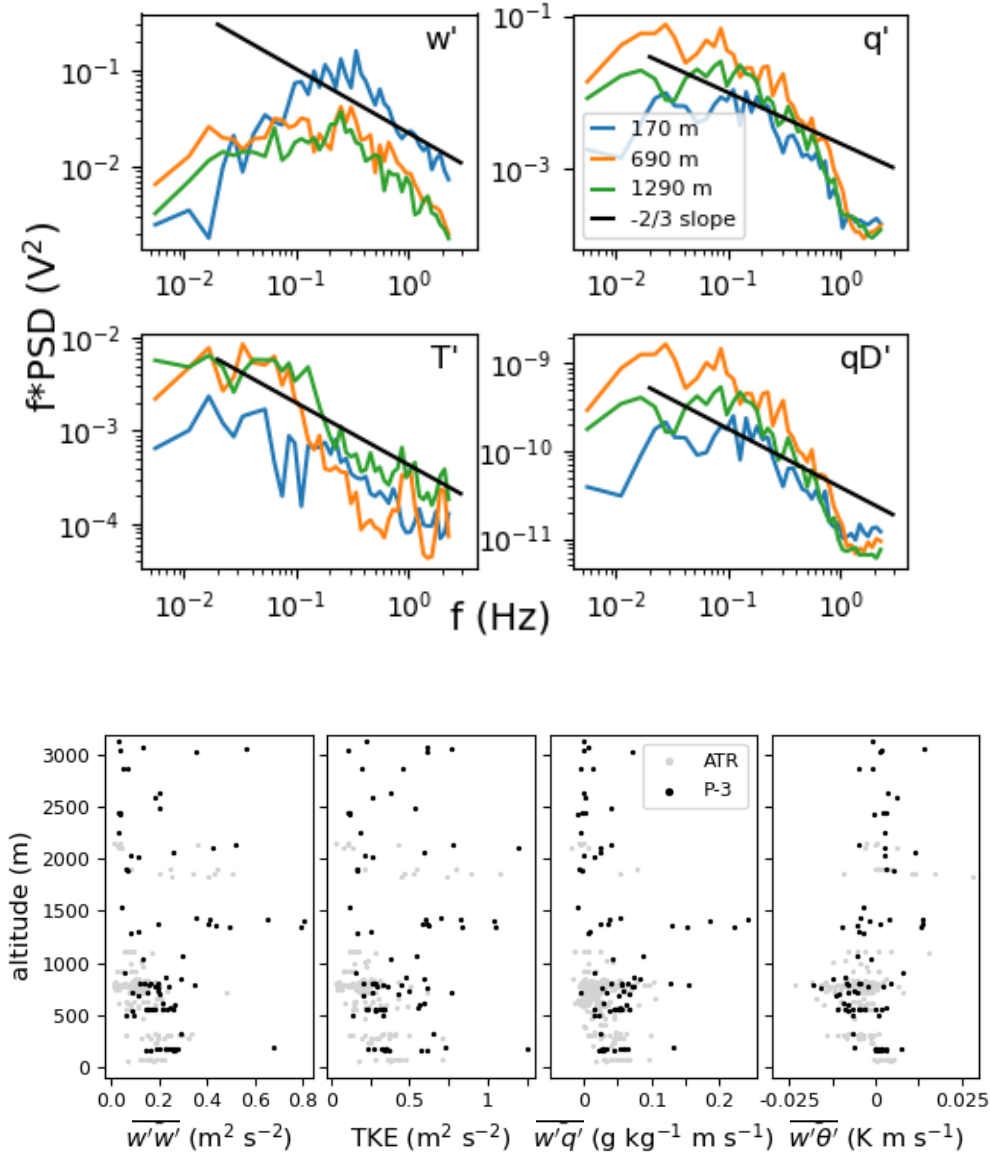


**Figure 3.** (Top) Frequency-weighted power spectral densities of  $w'$ ,  $q'$ ,  $\theta'$ , and  $qD'$  for 3 level legs of cloud module 04 (31 Jan 2020). (bottom) comparison of  $w'w'$ , TKE,  $w'q'$ , and  $w'\theta'$  from the P-3 to the SAFIRE ATR 42 aircraft long horizontal legs.

CAM6 uses the Zhang-McFarlane scheme to model deep convection (Zhang & McFarlane, 1995) and the Cloud Layers Unified by Binormals scheme (CLUBB, Bogenschutz et al., 2012; Golaz et al., 2002; Larson et al., 2002b) to model boundary layer turbulence, shallow convection, and cloud microphysics. Cloud microphysics are parameterized by the Morrison-Gettelman scheme, version 2 (Gettelman & Morrison, 2015; Morrison & Gettelman, 2008). Details of the water isotope physics in the atmospheric model are given in Nusbaumer et al. (2017), while parameterization of land-atmosphere isotope ratio exchanges are given in the appendix to Fiorella et al. (2021). CAM6 is used to obtain 3-hourly mean values of thermodynamic quantities and turbulence quantities from CLUBB.

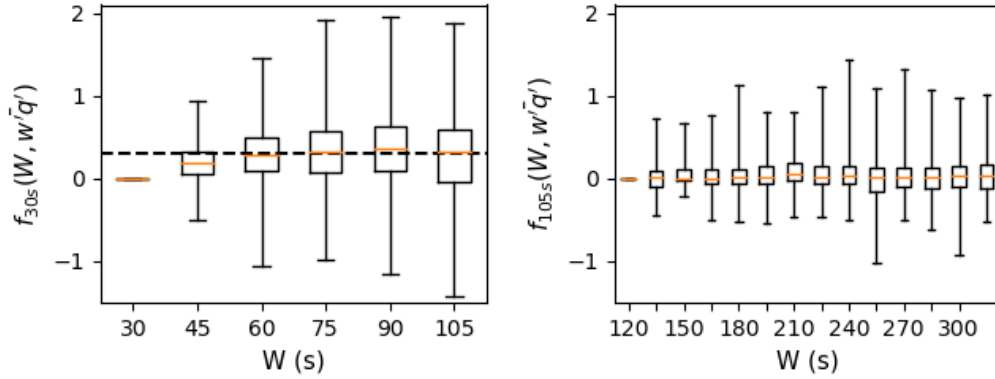


**Figure 4.** Box plot distributions of fraction change in  $\overline{w'q'}$  with window size for all level legs. (Left) Fractional changes from those computed with a 30 s window. (Right) Fraction changes from those computed using a 120 s window.

### 3 Results

#### 3.1 Synoptic conditions

Since the cloud modules span a range of latitudes and longitudes, two approaches are taken to assess synoptic and large-scale forcing: general time series over the P-3 study region are shown (Fig. 5) as well as values for  $2^\circ \times 2^\circ$  windows centered on each cloud module (Fig. 6). The window is chosen to match a P-3 dropsonde circle size. Dropsondes circles were an integral part of the campaign meant to capture the interplay between large scale forcing and cloud properties. ERA5 reanalysis data (hourly,  $0.25^\circ \times 0.25^\circ$  spatial resolution) is used for surface wind and pressure, 600 hPa vertical velocity, and lower tropospheric stability over the latitude range ( $10.5^\circ\text{N}$ ,  $15^\circ\text{N}$ ) and longitude range ( $-59^\circ\text{E}$ ,  $-52^\circ\text{E}$ ). LCLT S is computed from the 1000-600 hPa potential temperature difference. Wind shear is computed between surface and 700 hPa. For vertical velocity and LCLT S, the 600 hPa level is chosen to avoid cloud tops which at times were observed near 700 hPa. The divergence time series on the scale of the ATOMIC region (Fig. 5) is not shown here since the spatial variation over the study region is large in comparison to its mean value.

The study region is characterized by regional subsidence. There is clear anticorrelation between LCLT S and surface windspeed, with the beginning of observation period (OP) showing increasing LCLT S and decreasing  $U_{sfc}$  in the middle of January, then reversing February 03. A low pressure drop during January 21-25 (associate with an eastward propagating anomaly north of the study region, Fig. 5) coincides with two of the HCHT cases, but otherwise the cloud groupings evolve linearly from LCLT to HCHT throughout the OP.

For the  $2^\circ \times 2^\circ$  windows centered on each cloud module, the most effective variable pair to cluster the three cloud groups are low-level divergence (at 950 hPa) and surface wind speed (Fig. 6). LCLT and LCHT groups split by

surface windspeed, while the HCHT group is characterized by convergence. There is no correlation between large scale 600 hPa vertical velocity and surface divergence, and effective clustering is not achieved when using 600 hPa vertical velocity in place of divergence. Anticorrelation between  $U_{sfc}$  and LCLT S seen in the timeseries is also present in the windows, with a correlation of -0.81. Aside from the two HCHT cases during the low pressure drop,  $U_{sfc}$  and LCLT S produce clustering for the cloud groups. Bony et al., (2020) used surface windspeed and estimated inversion strength to similarly cluster cloud mesoscale organization. The small sampling statistics is a limiting factor for this study which must be kept in mind when generalizing the findings.

### 3.2 Observed boundary layer and turbulence structure

ML tops are located at 500 – 700 m (Fig. 2), with LCLs typically 0 – 200 m higher (cloud module 02 as the exception). Trade inversion bases are  $1540 \pm 100$  m,  $1600 \pm 160$  m, and  $2260 \pm 260$  m, respectively. Average cloud tops (as defined in Fig. 2) for each group are  $1800 \pm 320$  m,  $1860 \pm 170$  m, and  $2680 \pm 286$  m respectively. The ratio of average cloud top (as defined in Fig. 2)  $z_{ct}$  to trade inversion base  $z_{tib}$  is consistent among the groups,  $1.17 \pm 0.19$ ,  $0.17 \pm 0.04$ , and  $1.19 \pm 0.11$  respectively. Figure 7 shows mean profiles of  $\theta$ ,  $q$ ,  $RH$ , and  $dD$  for each cloud group. The ML regions show constant  $\theta$  and  $q$  with linearly increasing  $RH$ . Above the ML up to 1500 m,  $\theta$  follows a moist adiabatic lapse rate.  $RH$  shows an average 6% decrease from ML top and then remains roughly constant with height up to 1500 m. The lapse rate in  $q$  is initially  $1 \text{ g kg}^{-1}/100 \text{ m}$  ( $10 \text{ g kg}^{-1} \text{ km}^{-1}$ ) in the first 200 m above ML and then maintains an average, smaller, value of  $3.2 \text{ g kg}^{-1} \text{ km}^{-1}$  up to 1500 m. The difference in mean profiles of all variables up to 1500 m are not statistically significant between cloud groups. However, HCHT shows a slightly drier ML, as well as a more uniform  $q$  lapse rate with constant  $RH$  between ML top and 1500 m without the sharper gradients just above ML top, consistent with increased mixing between the sub-cloud and cloud layers that might be expected during stronger convective activity. The largest difference in the cloud groups occurs above 1500 m. LCLT and LCHT show distinct trade inversion bases around 1500 m where sharp gradients in  $\theta$ ,  $q$ , and  $RH$  occur while HCHT maintains similar lapse rates up to 2200 m. A trade inversion altitude of 1500 m is indistinguishable on average for LCLT and LCHT. Trade inversions for HCHT are weaker and occur between 2000 – 2200 m, demonstrating the effect of clouds and convection on the boundary layer structure.

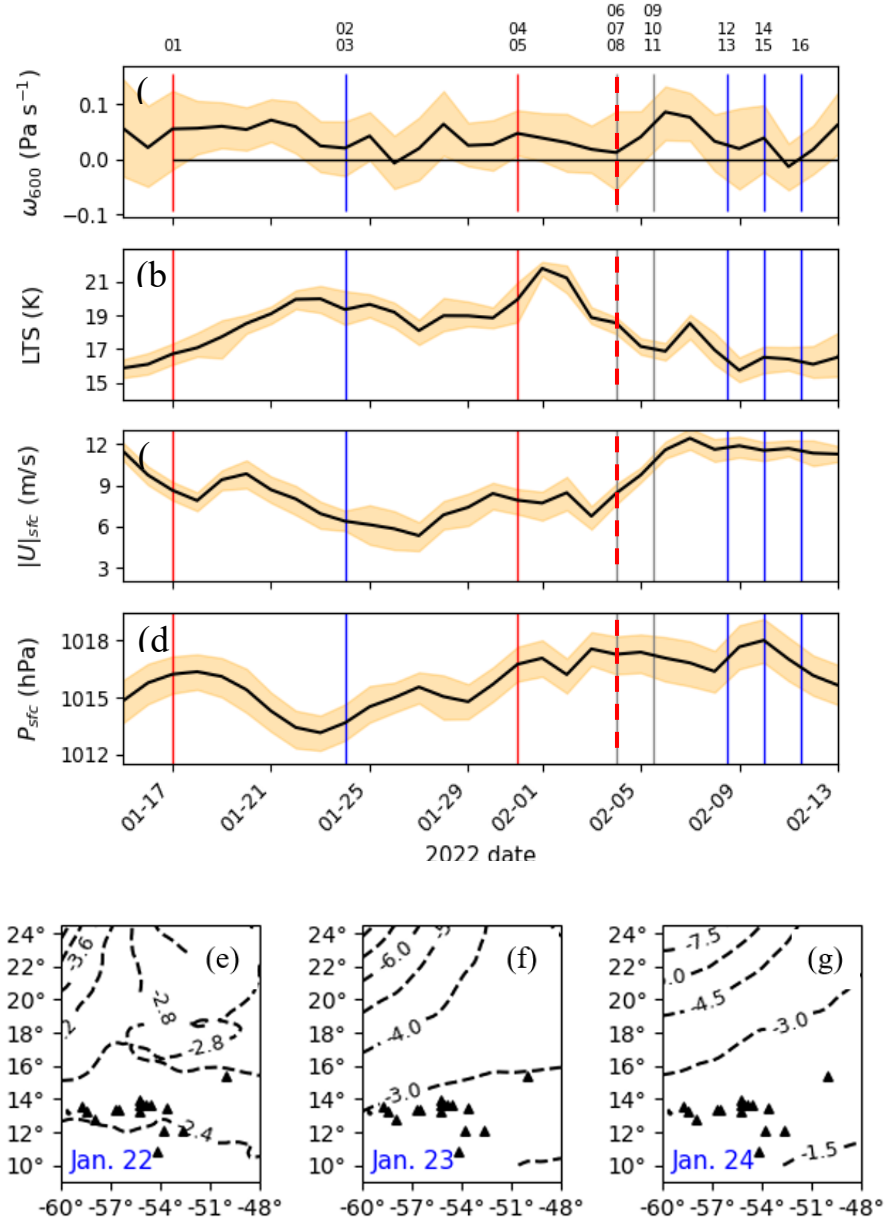


**Figure 5.** (a-d) Synoptic timeseries of (from top to bottom) 600 hPa vertical velocity, lower tropospheric stability, surface wind speed, and surface pressure during the P-3 OP. Cloud module numbers are marked on the days they took place (vertical lines). (e-g) Surface pressure anomalies (hPa) during Jan. 22-24 with P-3 cloud module sampling locations.

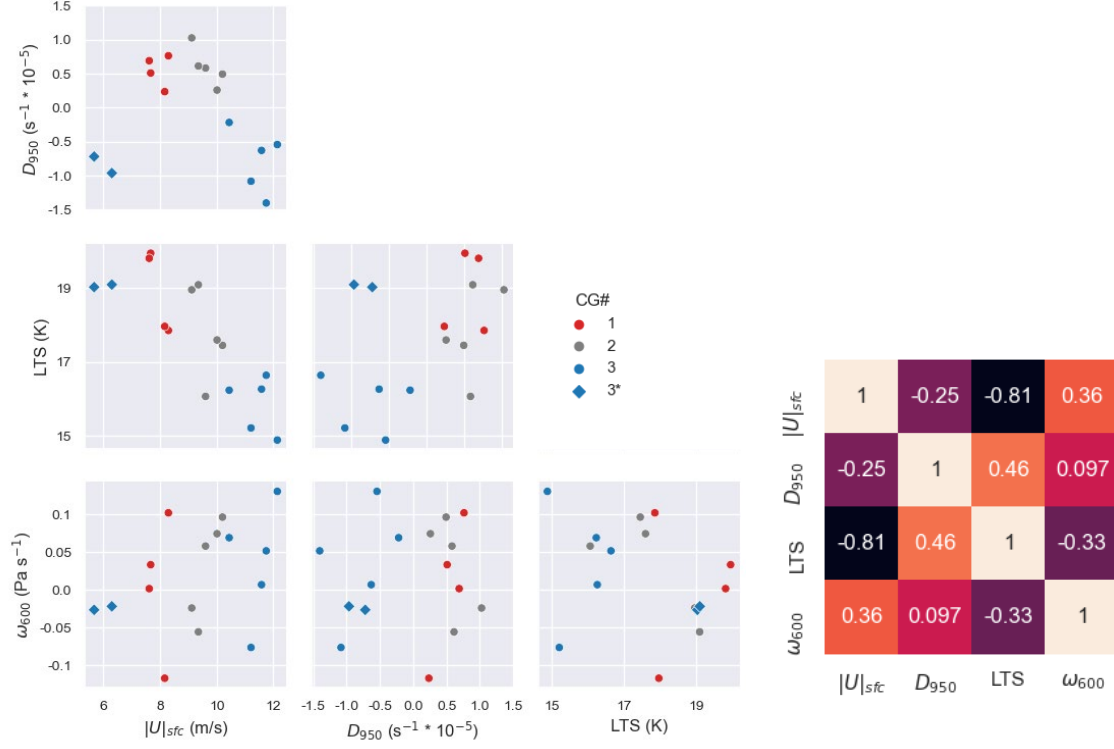


**Figure 6.** (Left) Large-scale circulation and forcing variable pairs from ERA5 during each P-3 cloud module, colored by cloud group. Each point represents a spatial / temporal average over a 2° x 2° window centered on the cloud module location and over the 3 hours leading to P-3 sampling. (Right) Cross-correlation matrix for large-scale circulation and forcing variables.

Despite the statistically insignificant differences in the thermodynamic profiles, the differences in turbulent and flux characteristics between cloud groups are significant from ML top to 1500 m (Fig. 8). LCLT has the lowest turbulence values, 2-4x smaller than for LCHT, and HCHT. Both LCHT and HCHT have maximum  $\overline{w'w'}$  around 0.3 – 0.35 m<sup>2</sup>s<sup>-2</sup>. LCLT also shows a local maximum in  $\overline{w'w'}$  at the same altitude as LCHT although it is smaller (0.125 m<sup>2</sup>s<sup>-2</sup>). The ratio of these local  $\overline{w'w'}$  maxima to median cloud top is 0.85, 0.75, and 0.77 for LCLT, LCHT, and HCHT respectively. Horizontal wind variance profiles show analogous features and distinctions between cloud groups to the vertical wind. In the ML, HCHT has 50% greater TKE<sub>h</sub> than the other two groups. This also leads to an anisotropy ratio  $2\overline{w'w'}/(\overline{u'u'} + \overline{v'v'})$  of 0.5 for HCHT, indicative of a degree of thermal stratification, while the other two cloud groups have values near 1 (associated with isotropic turbulence, typically an assumption for the sub-cloud layer). The anisotropy ratio for LCLT decreases with height above ML top while LCHT remains near isotropic up to 1500 m. The anisotropy ratio for HCHT shows a nearly inverse profile. Defining column integrated TKE in the lower 3 km as

$$TKE_{col} = \int_0^{3 \text{ km}} \rho \cdot TKE \cdot dz, \quad (7)$$

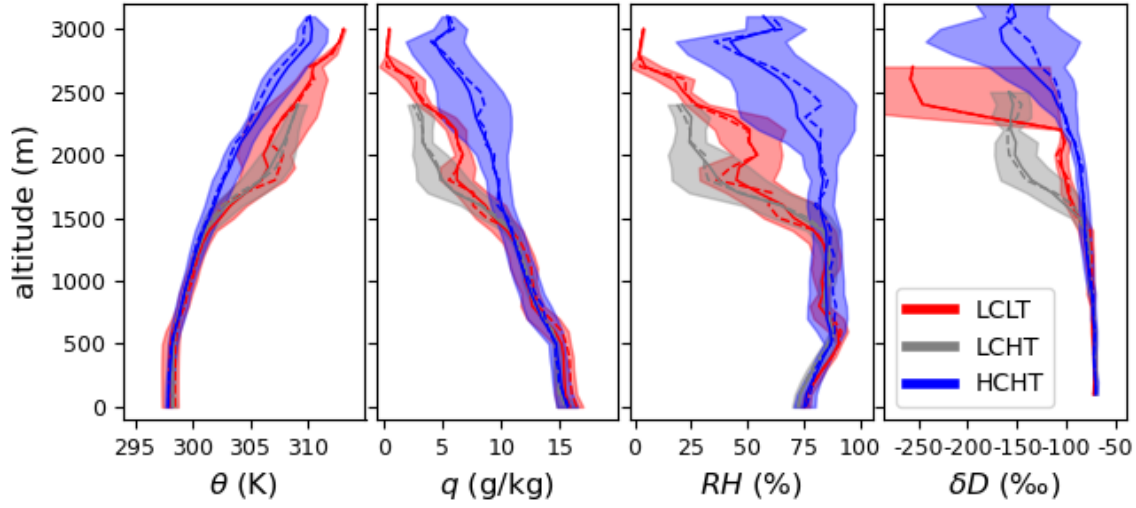


**Figure 7.** Thermodynamic profiles for each cloud group, including mean (solid), median (dashed), and min / max values (shaded). Potential temperature, water mixing ratio, and RH are derived from dropsondes.  $\delta D$  profiles derived from in-situ measurements.

with  $\rho$  the air density, values of 552, 952, and 1321 J m<sup>-2</sup> are obtained for the respective cloud groups. The majority of the difference between the groups comes from the horizontal component. The vertical component of  $TKE_{col}$  for each cloud group is 135, 272, and 292 J m<sup>-2</sup> respectively.

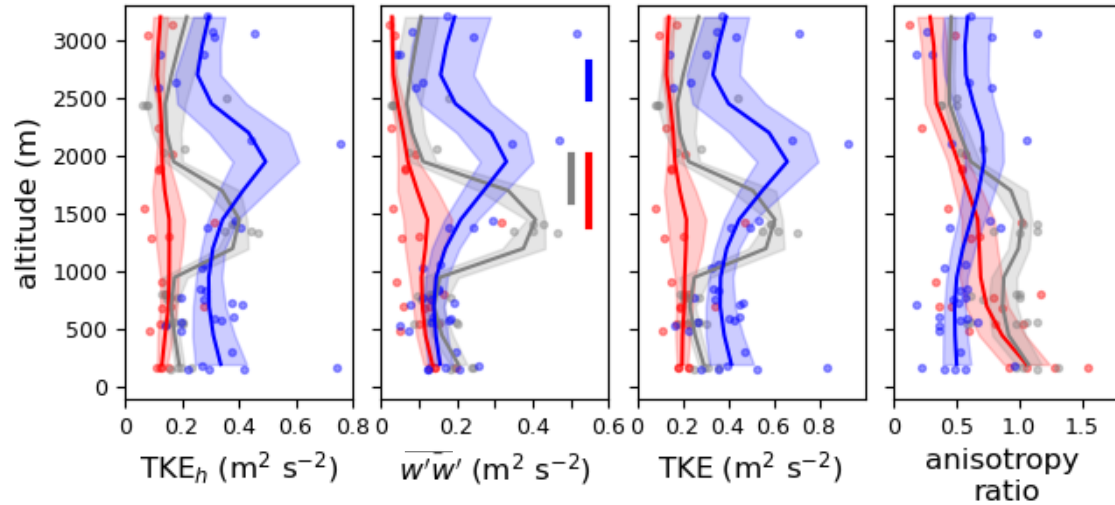


**Figure 8.** Vertical profiles of (left to right) horizontal kinetic energy,  $\overline{w'w'}$ , TKE, and anisotropy ratio from the P-3 measurements. Measurements are split by cloud group with the same coloring as in Fig. 6. Mean profiles (solid) and standard deviation on the mean (shaded) are derived from kernel density estimation.



Sensible heat flux (SHF) tends to be positive at around  $10 \text{ W m}^{-2}$  near the surface, reaches negative values above the ML, typically about  $5 \text{ W m}^{-2}$ , and is close to zero higher up. This result is also seen in Brilouet et al. (2021). SHFs between the cloud groups show no distinction at least below 2 km. However, latent heat fluxes (LHFs) do differ between the groups. LCLT has the smallest LHFs, in line with the smaller observed  $\overline{w'w'}$ . LCHT, with higher  $\overline{w'w'}$  and strong gradients in  $q$  near the trade inversion, has the highest LHFs at  $300 - 400 \text{ W m}^{-2}$ . While HCHT has similar column-integrated  $\overline{w'w'}$  to LCHT, the weaker gradients in  $q$  results in LHFs nearly constant at  $100 \text{ W m}^{-2}$  throughout the bottom 2 km. LHFs are similarly at  $100 \text{ W m}^{-2}$  in the ML for LCLT and HCHT with LCHT having values on average 25 – 50 % higher. There are positive buoyancy fluxes throughout the ML which approach 0 but increase further up. LCHT has the highest buoyancy flux values below 1500 m, connected to the large LHFs. HCHT has comparatively constant values throughout the column. LCLT is not statistically different than 0 above the ML.  $\delta D$  of the flux is also computed for the cloud groups. No statistically significant differences  $\delta D$  of the flux between the groups are below 2.5 km.

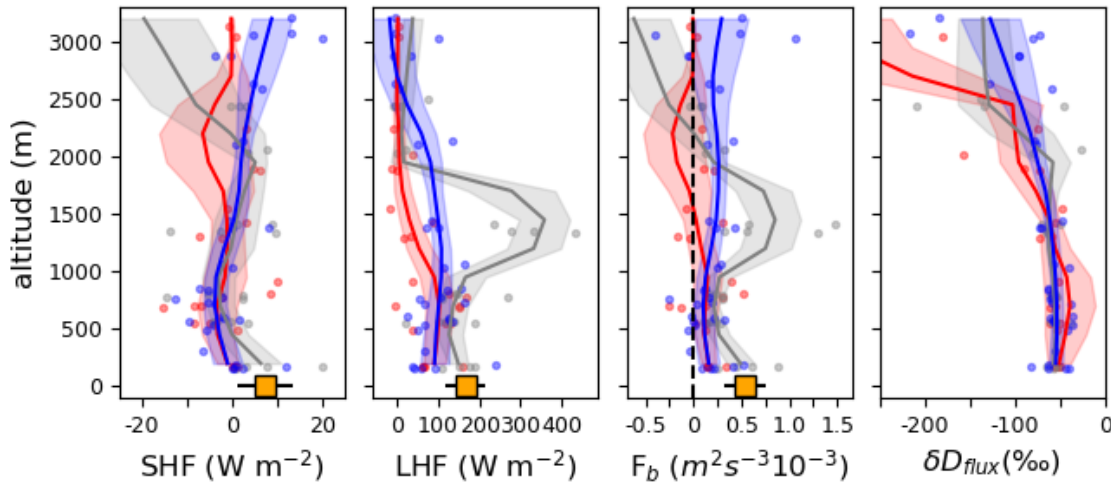


**Figure 9.** Analogous to Fig. 7 but for (left to right) SHF, LHF, buoyancy flux, and  $\delta D$  of the flux. Orange boxes are mean and standard deviation of R/V Ron Brown measurements from 17 January to 12 February, 2022.

### 3.3 CAM6 boundary layer and turbulence structure

Care needs to be taken when comparing CAM6 output to the small number of P-3 profiles. Being forced by ERA5 meteorology, statistics from CAM6 at the time and location of the aircraft cloud modules enable a direct evaluation of both the mean thermal state and the CLUBB covariance (flux) quantities. The horizontal length of the aircraft profiles (typically 100 km) is comparable to the nominal  $1^\circ$  resolution of the model. It was found that the mean

thermodynamic profiles ( $\theta$ ,  $q$ ,  $RH$ ,  $\delta D$ ) agree well with the observations (Fig. 10) and so they are presented in terms of the three cloud groups. This suggests these are captured by synoptic scale weather patterns for which CAM6 is accurately nudged towards. For the turbulence and flux quantities, CAM6 statistics over the ATOMIC region and for the collection of P-3 flight dates are represented by three sets of profiles (Fig. 11 and 4.12) that aim to capture the extremities of possible variation that one might expect within model grid cells:

- The mean profile over grid points in the blue box of Fig. 1, and over all times on flight dates in a given cloud group (referred to as  $\mu$  profiles).
- The mean of grid points with column integrated  $\overline{w'w'}$  in the lower 3 km above the 95<sup>th</sup> percentile (referred to as  $\mu_{95}$  profiles).
- The mean of grid points with column integrated  $\overline{w'w'}$  in the lower 3 km above the 99<sup>th</sup> percentile (referred to as  $\mu_{99}$  profiles).

The objective with these profiles is to get an understanding of the mean state as well as look at the higher end of turbulent activity in CAM6 (the latter is expected to correspond to cumulus clouds). Two sets of  $\mu$ ,  $\mu_{95}$ ,  $\mu_{99}$  are computed, one for the LCLT + LCHT flight dates (Fig. 11) and one for the HCHT flight dates (Fig. 12).

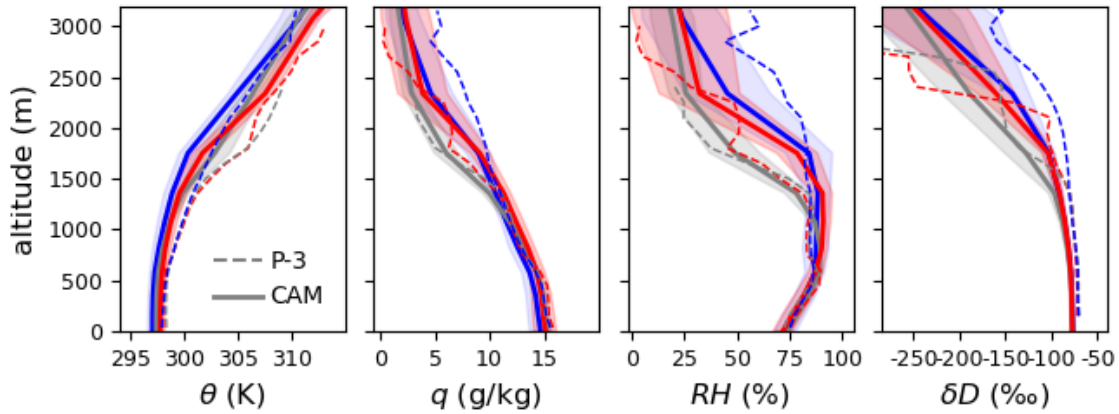


**Figure 10.** Thermodynamic structure for the CAM6 run, with the same cloud group coloring as in Fig. 6. Means (solid) and standard deviations of the mean (shaded) are shown. P-3 mean profiles are overlain (dashed).

Mean thermodynamic profiles of CAM6 output over the ATOMIC study region (Fig. 1) split by cloud group agree well with the observations. Although CAM6 tends to be 0.5 – 1 K cooler than the observations, mixed layer tops are placed correctly at 500 – 700 m. Trade inversion bottoms (evident in lapse rates of  $\theta$ ,  $q$ , and  $RH$ ) occur around 1500 m for LCLT and LCHT while HCHT follows a moist adiabatic lapse rate above 2 km. Even the elevated moisture

above the trade inversion base in LCLT is represented in CAM6. CAM6 is able to reproduce boundary layer structure both qualitatively and quantitatively when nudged by horizontal winds and surface pressure.

In the ML, the CLUBB scheme in CAM6 is able to simulate the range of observed  $\overline{w'w'}$  throughout the column, but produces smaller horizontal wind variances except near the surface. This results in CLUBB anisotropy ratios greater than 1 and greater than observed in the 200 – 700 m region. SHF is simulated well, while LHF tends to be overestimated by 150 – 200 %. The CLUBB ranges include the observations of  $\overline{w'w'}$  and LHF for LCLT. However, CLUBB underestimates horizontal TKE. Above the ML, the large increase in  $\overline{w'w'}$ , TKE, and LHF for LCHT observations are not simulated. Even the  $\mu_{99}$  maximum is only 50 % of that observed. CLUBB generates more turbulence and 2-3 x larger LHF on HCHT days than days for the other two groups, which is not observed but could potentially be sampling bias (e.g. by the time the aircraft reaches the clouds to be sampled, some of the turbulence has dissipated). The peak in CLUBB turbulence for HCHT is placed lower than the observations (1500 m rather than 2000 m). Above 2000 m, even the highest values of  $\overline{w'w'}$  and TKE in CLUBB do not reach those observed. That is, CLUBB tends to taper turbulence off to 0 too quickly, unless the fluxes at these levels are being passed off to the deep convection scheme.

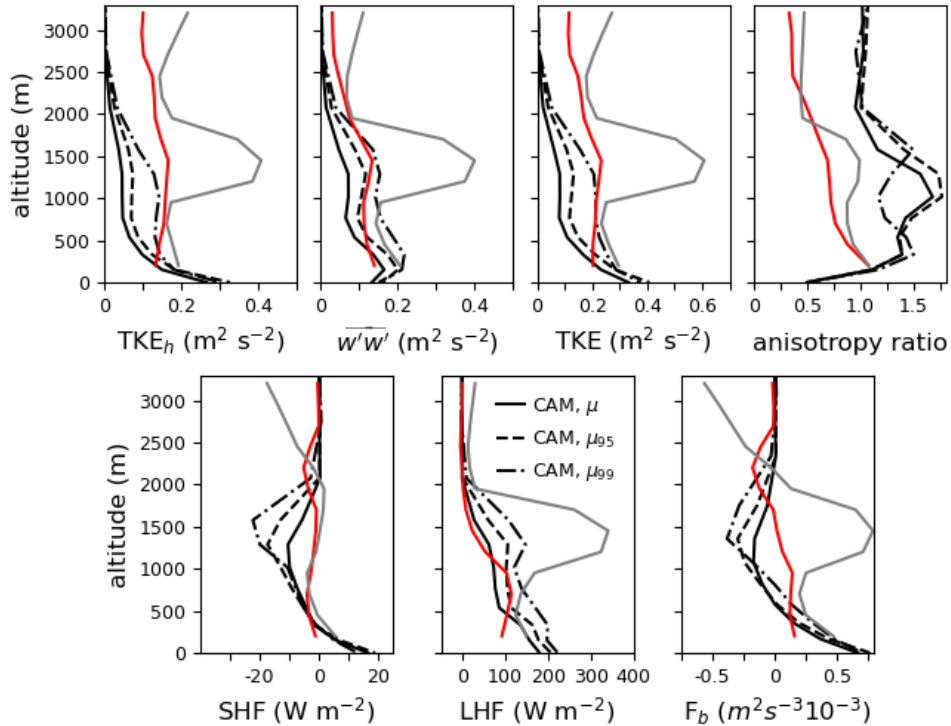


**Figure 11.** Turbulence and flux structure from CAM run for the collection of P-3 flight days in the LCLT and LCHT groups. Red, grey, and blue profiles are P-3 mean profiles with same cloud group coloring as in Fig. 6.

A clear discrepancy between CLUBB and the observations is the strongly negative SHF produced in CLUBB which are most negative near 1500 m (the trade inversion base for LCLT and LCHT). Strongly negative SHF is not observed for any cloud group, yet are present for all CLUBB profiles presented here. Higher column integrated  $\overline{w'w'}$  corresponds to more negative SHF. The strongly negative SHFs also result in strongly negative buoyancy fluxes near 1500 m, as opposed to the positive buoyancy fluxes seen from the P-3.

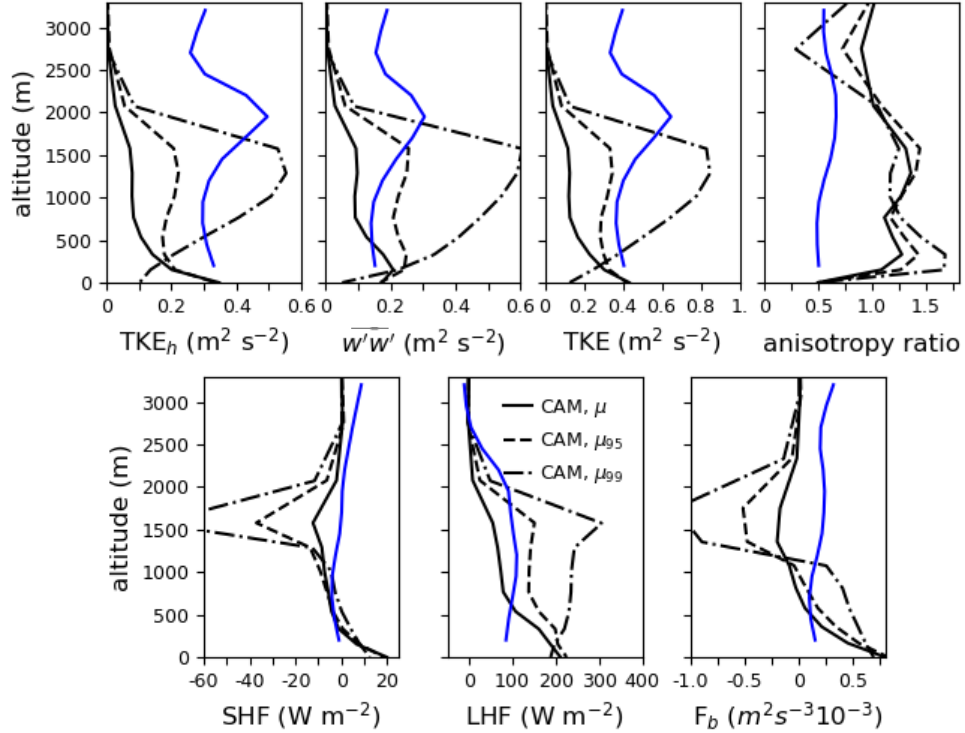


**Figure 12.** Analogous to Fig. 10 but only for HCHT flight dates.

## 4 Discussion

### 4.1 Observed thermodynamic, turbulence, and flux profiles

The 16 cloud modules from the P-3, consisting of stacked level legs throughout the sub-cloud and cloud regions, were split into three groups according to cloud top height and column-integrated TKE and vertical velocity variance, although it is observed that these groups map onto horizontal cloud size and clustering over a scale of 100 km. The same groupings can also be achieved through the surface windspeed and low-level divergence on the scale of a few hundred km. The low-level divergence distinguishes HCHT from the other two groups while surface wind speed separates LCLT from LCHT. The sampled cloud systems progress from LCLT to HCHT other than two HCHT

cases toward the beginning of the OP coinciding with an eastward propagating low pressure anomaly toward the north.

Consistent ratios of cloud top height, trade inversion base, and altitude of maximum turbulence are observed over the P-3 cloud modules. The ratio of cloud top  $z_{CT}$  to inversion base  $z_{TIB}$  is uniform across the groups at  $1.18 (\pm 10\%)$  even though mean  $z_{CT}$  is about 800 m greater for HCHT. The ratio of maximum  $\overline{w'w'}$  above the ML to cloud top is also uniform at around 0.75. The consistency may point to the underlying interaction between convection, dissipation, and entrainment mixing near cloud top, and how they interact with the ambient thermodynamic structure. For example, cloud heights not reaching more than 20 % of the trade inversion base may point to the maximum amount of convective available potential energy (CAPE) that can be produced in shallow cumulus systems under typical conditions. Previous studies looking at turbulence vertical structure have normalized by some height, often trade inversion base or lifting condensation level (e.g. Pennell and LeMone, 1974; Grant and Lock, 2004; Lareau, 2020; Dodson and Griswold, 2021), reflecting the utility of scale-independent turbulence structure. In comparison to the stratocumulus-topped marine boundary layers investigated in Dodson and Griswold (2021), the observed altitudes of peak turbulence as a fraction of cloud top height are smaller (0.75 here vs 0.89 in their results). However, stratocumulus cloud layers are typically thinner than trade cumulus layers and capped by much stronger trade inversions, so the dynamics may differ.

The mean thermodynamic profiles between the groups do not differ with statistical significance below 1500 m, which is within 100 m of the mean trade inversion base for LCLT and LCHT. The only difference occurs above 1500 m, where HCHT is distinguished from the other cloud groups, clearly reflective of the increased convective activity. Despite similar boundary layer structure of  $\theta$ ,  $q$ , and  $RH$  below 1500 m, the turbulence structure of the three groups are different. LCLT has the smallest  $\overline{w'w'}$  and TKE values, which taper from surface values to 0 and  $0.1 \text{ m}^2 \text{ s}^{-2}$  respectively with height. LCHT has 2x the column integrated TKE and vertical velocity variance of LCLT. Likewise HCHT has 2x the column integrated vertical velocity variance and 2.5x the column integrated TKE as LCLT. A key difference between HCHT and LCHT is the increased horizontal TKE present in the sub-cloud ML and most of the overlying column. Mean values in the ML are on average 70% higher ( $0.18$  vs  $0.31 \text{ m}^2 \text{ s}^{-2}$ ). One candidate for the increased  $\text{TKE}_h$  is cold pools (a key investigation topic in EUREC<sup>4</sup>A-ATOMIC). Since cold pools fronts propagate in directions not necessarily aligned with the mean wind, they would generate higher observed  $\text{TKE}_h$ . The increased variance may also be associated with the observed surface convergence for HCHT.

The fact that the turbulence structure varies between the cloud groups but thermodynamic structure does not points to the importance of understanding conditions which lead to the former. That is, thermodynamic structure may not be a good predictor of the cloud characteristics, and other quantities should be focused on such as moisture convergence. Figure 13 provides a summary schematic of the differences in turbulence between the cloud groups and offers a perspective on how progression from LCLT to LCHT and HCHT might occur. Light surface winds and turbulence which decreases from the ML with height generates clouds with generally uniform spacing and smaller features (panel a). As the surface winds increase, convective aggregation occurs (panel b). If this leads to a large

divergence in LHF in the column overlying the ML, cloud breakup may occur. Finally, if surface convergence occurs, convection and turbulence reach higher altitudes, producing higher clouds which may precipitate and create cold pools. The convective activity is strong enough to alter the mean thermodynamic structure of the boundary layer, and the trade inversion deepens and weakens. The progression need not be linear from LCLT through to HCHT. For example, if cloud break up occurs during LCHT leading to clear air, the boundary layer could revert to a low turbulence state characteristic of LCLT.

The transport of moisture in the lower few km of the atmosphere is a key challenge for understanding of shallow cloud boundary layers, and therefore assessing fluxes over this region is equally important yet uncommon. For LCHT, the large  $\overline{w'w'}$  values combined with sharp gradients in  $q$  lead to LHF of 250-400 W m<sup>-2</sup> near  $z_{TIB}$  in some cases, which is comparable growing PBLs over land (Lareau 2020). There is strong divergence of LHF in the altitude region 800 – 1400 m, which would lead to drying of the layer if compensating moisture convergence is not present, something also discussed by Lareau (2020). Assessment of GOES-16 reflectance videos show that for cloud modules 6, 7, and 10 (all in the LCHT group), the cloud clearly breaks up either during or within an hour after P-3 sampling. From 1400 – 2000 m, there is convergence of moisture, suggesting that the cloud is moistening the troposphere above the inversion layer. For HCHT, surface convergence is present, which may provide the moisture necessary to maintain clouds. Despite higher clouds in HCHT than LCHT, both have the same column integrated TKE and  $\overline{w'w'}$ . This may be associated with the timing of aircraft sampling. For example, Katzwinkel et al. (2014), investigate the turbulent and buoyancy characteristics of shallow cumuli in three categories based on cloud properties: actively growing, decelerated, and dissolving. In ATOMIC, the locations of cloud modules were chosen by identifying cloudy areas via satellite imagery and then transiting to the identified location. It is possible that by the time the sampling location was chosen and sampled, a portion of the turbulence resulting from the higher clouds had dissipated.

## 4.2 Comparison of observations with CAM6

Cloud modules in the HCHT group occurred during surface convergence which presumably led to the higher clouds observed on those days. Since CAM6 is nudged by winds and surface pressure, the daily variation of large-scale circulation should be captured. The CLUBB scheme in CAM6 produces 2-3 x higher column integrated TKE,  $\overline{w'w'}$ , and LHF on these days. However, CLUBB simulates peaks in these quantities at 1500 m, which is 500 m lower than the observations. Whether or not this is indicative of CLUBB representation of the convection, the trade inversion, and penetrative entrainment requires further investigation. One explanation for the discrepancy is that grid points with column integrated  $\overline{w'w'}$  larger than the 95<sup>th</sup> and 99<sup>th</sup> percentiles represent the growing clouds, whereas the observations may sample them after the TKE has dissipated somewhat (e.g. the concept explored above). However, repeating the analysis with e.g. the 90<sup>th</sup> percentile of column integrated  $\overline{w'w'}$  still places the maximum turbulence at around 1500 m. Another possibility is that the deep convection scheme (Zhang and McFarlane, 1995) is being

triggered in CAM6 and producing excessive vertical heat and water transport, which then triggers CLUBB to provide (non-physical) compensation via downward SHF.

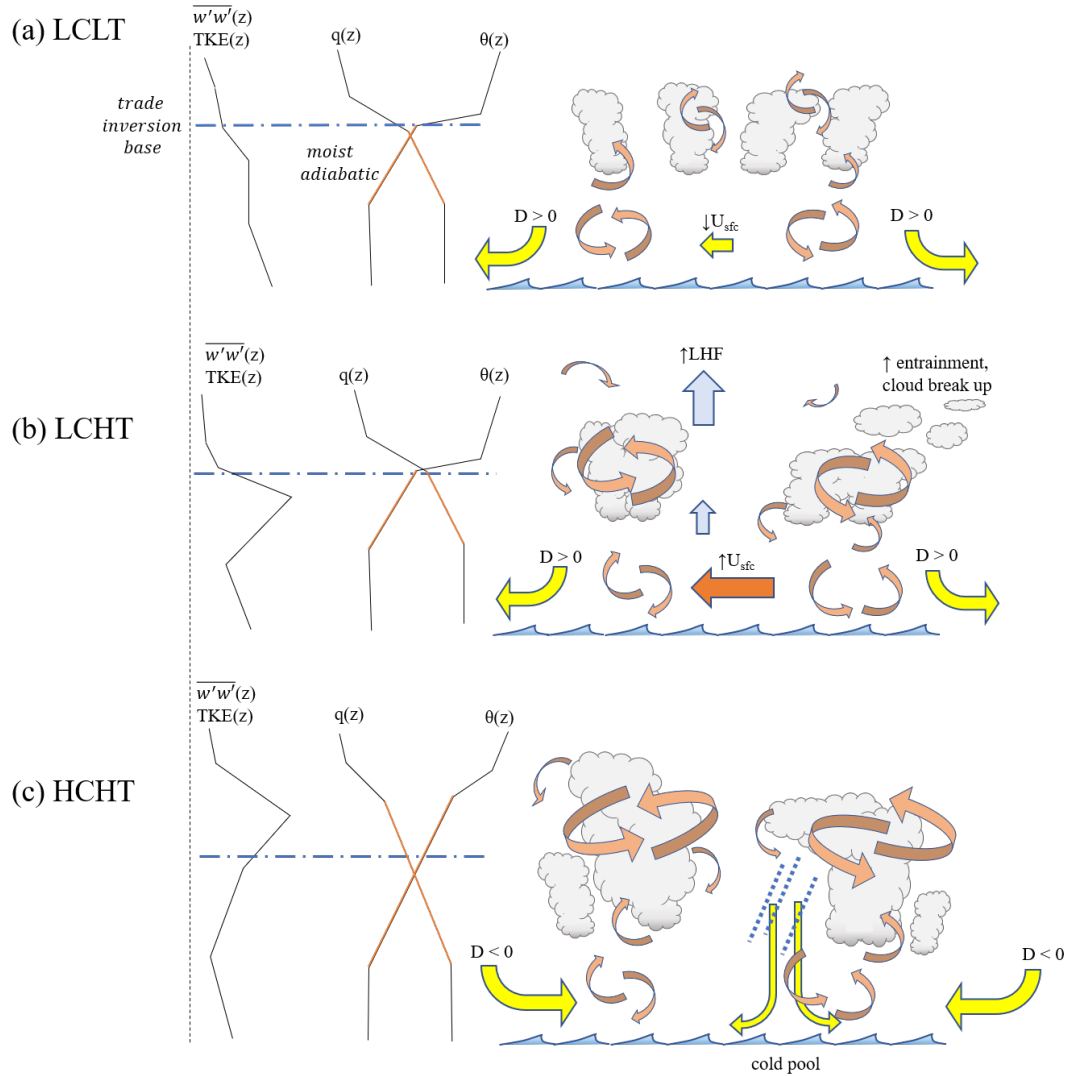


**Figure 13.** Schematic of the hypothesized coupling between large-scale circulation, turbulence and thermodynamic structure, and cloud characteristics (cloud top heights and horizontal organization).

Large TKE,  $\overline{w'w'}$ , and LHF values between the ML and trade inversion base are seen in LCHT observations but not simulated in CAM6. While the column integrated  $\overline{w'w'} \mu_{99}$  profiles have small local maxima placed at the correct altitude, the simulated magnitude is 2-2.5x smaller than those observed. The smaller LHF at trade inversion base could also lead to an underestimation of free tropospheric moistening under conditions of large-scale subsidence and

surface divergence. Because this discrepancy is seen in  $\overline{w'w'}$  as well as LHF it is related to the representation of turbulent transport in the subgrid scheme rather than downgradient diffusion of  $q$  across the inversion. This could indicate that convective aggregation is not captured when estimating higher moments of  $w'$  in the CLUBB scheme. Alternately, since CLUBB is not responsible for deep convection (which is handled by the Zhang-McFarlane scheme) the handoff of shallow to deep convection would not be accounted for by the CLUBB turbulent statistics analyzed here.

The largest discrepancy between CAM6 and the observations is the strongly negative SHFs produced in CAM6 near 1500 m. Negative SHF indicates relatively cool air rising and relatively warm air sinking. The most negative SHFs are occur near the trade inversion base which points to higher potential temperature air across the trade inversion mixing downward. This in turn would suggest that the way in which CAM6 represents penetrative entrainment at trade inversion base is inaccurate and possibly obfuscated by the pairing of inconsistent treatment of shallow and “deep” clouds. The negative SHFs are large enough that the net buoyancy flux is also negative despite positive LHF. The observations on the other hand show net positive buoyancy fluxes. Again, this may be due to fluxes present in the deep convection scheme, which would bring cloudy air following a near moist adiabatic lapse rate through the trade inversion. Therefore, determining whether or not deep convection is being triggered in the shallow cumulus regime is necessary for comprehensive model-observation comparisons to be performed.

## 5 Final Remarks

The EUREC<sup>4</sup>A-ATOMIC campaign included 16 cloud modules with the WP-3D Orion aircraft. This study uses the cloud modules to derive aircraft vertical profiles of trade cumulus turbulence and fluxes from the sub-cloud ML to cloud tops. The profiles are placed in the context of large-scale circulation (surface divergence and windspeed) and cloud characteristics (mesoscale organization and cloud top height). This study provides one of few examples of full profiles of turbulence and fluxes in the trade cumulus boundary layer. Further, to the author’s knowledge this study presents the first assessment of profiles in the context of cloud organization. Finally, a CAM run during the ATOMIC study period provides a valuable comparison of turbulence and fluxes.

Grouping of cloud modules via their qualitative cloud horizontal characteristics explains well their turbulence profiles ( $\overline{w'w'}$  and TKE). Cloud fields with numerous small features have the least amount of turbulence, usually largest near surface and decreasing with height. Cloud fields that show aggregation (e.g. less uniform distribution of clouds, more frequent regions of cloudless air) show a large increase in turbulence in the region from ML top to trade inversion bottom. The peak of the turbulence occurs at close to 75% of the cloud top heights. Lastly, deeper clouds correspond to turbulence maxima at higher altitudes (although remaining at ~75 % of cloud top height) and an increase in TKE due to the horizontal component. The same grouping of cloud modules is also achieved quantitatively by surface wind speed and 950 hPa divergence, suggesting that these may be the two large scale circulation features most coupled with cloud characteristics and turbulence.



There are several noteworthy features of the turbulence and flux structure. For LCHT, high LHF near trade inversion base are observed, reaching  $300 - 400 \text{ W m}^{-2}$ . Since LHF at ML top are only  $150 \text{ W m}^{-2}$  on average, there is vertical divergence of moisture flux in this layer. If there is not sufficient compensation of horizontal moisture divergence, this layer would dry out, and in fact it was observed for several of the LCHT modules that the sampled clouds dissipated either during or soon after sampling. While ML turbulence is close to isotropic for LCLT and LCHT, it is around 0.5 for HCHT. One hypothesis is that the formation of cold pools from deeper, more frequently precipitating clouds leads to gust fronts which increase horizontal wind variability. Alternately,  $\overline{w'w'}$  could be suppressed due to stratification.

Lastly, a CAM6 simulation is run over the study period, nudged by ERA5 winds and surface pressure. CAM6's turbulence and shallow convective scheme, CLUBB, produces higher column integrated turbulence and larger maximum values during the HCHT days, which makes sense since these days are characterized by deeper clouds. However, the CLUBB turbulence peak is 500 m lower than observed. While 500 m is about the vertical resolution of CAM6 at this altitude, the discrepancy is consistent, suggesting there is a key bias in CLUBB representation of turbulence and moisture transport due to shallow convection. CAM6 also does not capture the large LHF seen for LCHT, which could result in insufficient lower free tropospheric moistening in the model during this type of cloud organization. The negative SHFs produced in CAM near 1500 m for all cloud groups is not observed in measurements from either the P-3 or ATR. Since this leads to a net negative buoyancy flux not observed, understanding why CAM produces this negative SHF merits further investigation but may have to do with CLUBB  $\overline{w'\theta'}$  not including mesoscale circulations or flux due to deep convection. The divergence of the CLUBB SHF shown here could be an artifact of handing off nearly continuous flux from the top of shallow clouds to the base of deep convection handled by the Zhang-McFarlane scheme. However, at minimum it can be concluded that relying on CLUBB as the only mechanism for vertical transport of moisture and heat in the trade cumulus region would produce results qualitatively and quantitatively different than those observed.

## Appendix: Fast wind processing

Evaluating the fluxes and wind structure using the WP-3D data required reprocessing data streams from the fast (FST) datafiles to derive a high-frequency wind estimate. To do so, variables from different sensors were resampled to a common 50 Hz resolution, including true airspeed (TAS), GPS velocities, differential pressures from the pressure probe integrated into the WP-3D's nosecone, and ambient temperature, pressure, and humidity. Aircraft attitude (pitch, roll, yaw) was already provided at 50 Hz. Aircraft angle of attack ( $\alpha$ ) and sideslip angle ( $\beta$ ) were derived using differential pressures from the nosecone pressure array and calibration coefficients provided by NOAA as follows:

$$\alpha = 0.122351 + 6.027304 \left( \frac{PD_\alpha}{PQ_\alpha} \right), \quad (\text{A.1})$$

$$\beta = 0.214857 + 7.108151 \left( \frac{PD_\beta}{PQ_\beta} \right), \quad (\text{A.2})$$

where  $PD_\alpha$  and  $PQ_\alpha$  are the differential pressure between the vertically-oriented pressure ports and the dynamic attack pressure, respectively, and  $PD_\beta$  and  $PQ_\beta$  are the differential pressure between the horizontally-oriented pressure ports and the dynamic slip pressure. Due to sensor noise, a 100-sample moving mean was applied to the TAS timeseries. In addition, initial evaluation of winds revealed a misalignment between different variables used for wind estimation, resulting in increased spectral noise at specific frequencies. To correct for this, aircraft pitch, roll and yaw were shifted backwards by 47 datapoints (slightly less than one second), while GPS velocities were shifted backwards by 27 datapoints (slightly more than half of a second). These numbers were determined by evaluating the cross-correlation between variables.

After these adjustments, three-component winds were estimated using equations originally presented in Lenschow (1986):

$$u = v_{Ag} - |U_a|D^{-1}[(\cos \theta \sin \psi) + \tan \beta (\sin \phi \sin \theta \sin \psi + \cos \phi \cos \psi) + \tan \alpha (\cos \phi \sin \theta \sin \psi - \sin \phi \cos \psi)], \quad (\text{A.3})$$

$$v = u_{Ag} - |U_a|D^{-1}[(\cos \theta \cos \psi) + \tan \beta (\sin \phi \sin \theta \cos \psi + \cos \phi \sin \psi) + \tan \alpha (\cos \phi \sin \theta \cos \psi - \sin \phi \sin \psi)], \quad (\text{A.4})$$

$$w = -w_{Ag} + |U_a|D^{-1}[(-1 \sin \theta) + \tan \beta (\sin \phi \cos \theta) + \tan \alpha (\cos \phi \cos \theta)], \quad (\text{A.5})$$

where  $u$ ,  $v$ , and  $w$  are the wind components in the east, north and upward orientation, respectively,  $u_{Ag}$ ,  $v_{Ag}$ , and  $w_{Ag}$  are the inertial velocities from the onboard GPS (east, north, and down, respectively),  $|U_a|$  is the aircraft TAS,  $\theta$ ,  $\phi$ , and  $\psi$  are the aircraft pitch, roll and yaw, respectively.  $D$  is a normalization factor, defined as:

$$D = \sqrt{1 + \tan^2 \alpha + \tan^2 \beta}. \quad (\text{A.6})$$

## References

- Arakawa, A., and W. H. Schubert, 1974: Interaction of a cumulus cloud ensemble with the large-scale environment, Part I. *J. Atmos. Sci.*, 31, 674–701, doi: 10.1175/1520-0469(1974)031<0674:IOACCE.2.0.CO;2.
- Bailey, A., Aemisegger, F., Villiger, L., Los, S. A., Reverdin, G., Quiñones Meléndez, E., Acquistapace, C., Baranowski, D. B., Böck, T., Bony, S., Bordsdorff, T., Coffman, D., de Szoeke, S. P., Diekmann, C. J., Dütsch, M., Ertl, B., Galewsky, J., Henze, D., Makuch, P., Noone, D., Quinn, P. K., Rösch, M., Schneider, A., Schneider, M., Speich, S., Stevens, B., and Thompson, E.: Isotopic measurements in water vapor, precipitation, and seawater during EUREC<sup>4</sup>A, *Earth Syst. Sci. Data Discuss.* [preprint], <https://doi.org/10.5194/essd-2022-3>, in review, 2022.

Bechtold, P., C. Fravalo, and J. P. Pinty, 1992: A model of marine boundary-layer cloudiness for mesoscale applications. *J. Atmos. Sci.*, 49, 10.1175/1723–1744, doi: 10.1175/1520-0469(1992)049,1723:AMOMBL.2.0.CO;2.

Bedka, K., Palikonda, R. 2018. GOES-16 Satellite Cloud Products Data. Version 1.0. UCAR/NCAR - Earth Observing Laboratory. <https://doi.org/10.5065/D6PN94FK>.

Bogenschutz, P. A., Gettelman, A., Morrison, H., Larson, V. E., Schanen, D. P., Meyer, N. R., & Craig, C. (2012). Unified parameterization of the planetary boundary layer and shallow convection with a higher-order turbulence closure in the Community Atmosphere Model: single-column experiments. *Geoscientific Model Development*, 5(6), 1407–1423. <https://doi.org/10.5194/gmd-5-1407-2012>

Bougeault, P., 1981a: Modeling the trade-wind cumulus boundary layer. Part I: Testing the ensemble cloud relations against numerical data. *J. Atmos. Sci.*, 38, 2414–2428, doi:10.1175/1520-0469(1981)038,2414:MTTWCB.2.0.CO;2.

Bougeault, P., 1981b: Modeling the trade-wind cumulus boundary layer. Part II: A higher-order one-dimensional model. *J. Atmos. Sci.*, 38, 2429–2439, doi: 10.1175/1520-0469(1981)038,2429:MTTWCB.2.0.CO;2.

Bolton, David. "The Computation of Equivalent Potential Temperature". *Monthly Weather Review* 108.7 (1980): 1046-1053. [https://doi.org/10.1175/1520-0493\(1980\)108<1046:TCOEPT>2.0.CO;2](https://doi.org/10.1175/1520-0493(1980)108<1046:TCOEPT>2.0.CO;2)

Bony S, Dufresne JL (2005) Marine boundary layer clouds at the heart of tropical cloud feedback uncertainties in climate models. *Geophys Res Lett* 32(L20):806. doi:10.1029/2005GL023,851

Bony, S., Stevens, B., Ament, F. et al. EUREC<sup>4</sup>A: A Field Campaign to Elucidate the Couplings Between Clouds, Convection and Circulation. *Surv Geophys* 38, 1529–1568 (2017). <https://doi.org/10.1007/s10712-017-9428-0>

Bony, S., Schulz, H., Vial, J., & Stevens, B. (2020). Sugar, gravel, fish and flowers: Dependence of mesoscale patterns of trade-wind clouds on environmental conditions. *Geophysical Research Letters*, 48, e2019GL085988. <https://doi.org/10.1029/2019GL085988>

Brilouet, P.-E., Lothon, M., Etienne, J.-C., Richard, P., Bony, S., Lernoult, J., Bellec, H., Vergez, G., Perrin, T., Delanoë, J., Jiang, T., Pouvesle, F., Lainard, C., Cluzeau, M., Guiraud, L., Medina, P., and Charoy, T.: The EUREC<sup>4</sup>A turbulence dataset derived from the SAFIRE ATR 42 aircraft, *Earth Syst. Sci. Data*, 13, 3379–3398, <https://doi.org/10.5194/essd-13-3379-2021>, 2021.

Cuijpers, J.W.M., Duynkerke, P.G., Nieuwstadt, F.T.M., 1996. Analyses of variance and flux budgets in cumulus topped boundary layers. *Atmospheric Research* 40, 307 – 337.

Danabasoglu, G., Lamarque, J. -F., Bacmeister, J., Bailey, D. A., DuVivier, A. K., Edwards, J., et al. (2020). The Community Earth System Model Version 2 (CESM2). *Journal of Advances in Modeling Earth Systems*, 12(2). <https://doi.org/10.1029/2019MS001916>

Dodson, D. S. and Small Griswold, J. D.: Turbulent and boundary layer characteristics during VOCALS-REx, *Atmos. Chem. Phys.*, 21, 1937–1961, <https://doi.org/10.5194/acp-21-1937-2021>, 2021.

Fiorella, R. P., Siler, N., Nusbaumer, J., & Noone, D. C. (2021). Enhancing Understanding of the Hydrological Cycle via Pairing of Process-Oriented and Isotope Ratio Tracers. *Journal of Advances in Modeling Earth Systems*, 13(10). <https://doi.org/10.1029/2021MS002648>

George, G., Stevens, B., Bony, S., Pincus, R., Fairall, C., Schulz, H., Kölling, T., Kalen, Q. T., Klingebiel, M., Konow, H., Lundry, A., Prange, M., and Radtke, J.: JOANNE: Joint dropsonde Observations of the Atmosphere in tropical North atlantic meso-scale Environments, *Earth Syst. Sci. Data*, 13, 5253–5272, <https://doi.org/10.5194/essd-13-5253-2021>, 2021.

Gettelman, A., & Morrison, H. (2015). Advanced Two-Moment Bulk Microphysics for Global Models. Part I: Off-Line Tests and Comparison with Other Schemes. *Journal of Climate*, 28(3), 1268–1287. <https://doi.org/10.1175/JCLI-D-14-00102.1>

Golaz, J.-C., Larson, V. E., & Cotton, W. R. (2002). A PDF-Based Model for Boundary Layer Clouds. Part I: Method and Model Description. *Journal of the Atmospheric Sciences*, 59(24), 3540–3551. [https://doi.org/10.1175/1520-0469\(2002\)059<3540:APBMFB>2.0.CO;2](https://doi.org/10.1175/1520-0469(2002)059<3540:APBMFB>2.0.CO;2)

Grant, A.L.M. and Lock, A.P. (2004), The turbulent kinetic energy budget for shallow cumulus convection. *Q.J.R. Meteorol. Soc.*, 130: 401-422. <https://doi.org/10.1256/qj.03.50>

Grinnell, Scott A., Christopher S. Bretherton, Alistair M. Fraser, and David E. Stevens. "Vertical Mass Flux Calculations in Hawaiian Trade Cumulus Clouds from Dual-Doppler Radar". *Journal of Atmospheric Sciences* 53.13 (1996): 1870-1886. [https://doi.org/10.1175/1520-0469\(1996\)053<1870:VMFCIH>2.0.CO;2](https://doi.org/10.1175/1520-0469(1996)053<1870:VMFCIH>2.0.CO;2).

Hersbach, H., Bell, B., Berrisford, P., Hirahara, S., Horányi, A., Muñoz-Sabater, J., et al. (2020). The ERA5 global reanalysis. *Quarterly Journal of the Royal Meteorological Society*, 146(730), 1999–2049. <https://doi.org/10.1002/qj.3803>

Henze, D., Noone, D., and Toohey, D.: Aircraft measurements of water vapor heavy isotope ratios in the marine boundary layer and lower troposphere during ORACLES, *Earth Syst. Sci. Data*, 14, 1811–1829, <https://doi.org/10.5194/essd-14-1811-2022>, 2022.

Huang, M., Xiao, H., Wang, M., & Fast, J. D. (2020). Assessing CLUBB PDF closure assumptions for a continental shallow-to-deep convective transition case over multiple spatial scales. *Journal of Advances in Modeling Earth Systems*, 12, e2020MS002145. <https://doi.org/10.1029/2020MS002145>.

Katzwinkel, Jeannine, Holger Siebert, Thijs Heus, and Raymond A. Shaw. "Measurements of Turbulent Mixing and Subsiding Shells in Trade Wind Cumuli". *Journal of the Atmospheric Sciences* 71.8 (2014): 2810-2822. <<https://doi.org/10.1175/JAS-D-13-0222.1>>.

Khairoutdinov, M. F. and D. A. Randall, 2003: Cloud resolving modeling of the ARM summer 1997 IOP: Model formulations, results, uncertainties, and sensitivities. *J. Atmos. Sci.*, 60, 607–625, doi: 10.1175/1520-0469(2003)060,0607:CRMOTA.2.0.CO;2.

Kollias, Pavlos and Bruce. A. Albrecht. "Vertical Velocity Statistics in Fair-Weather Cumuli at the ARM TWP Nauru Climate Research Facility." *Journal of Climate* 23 (2010): 6590-6604.

Krueger, S. K., 1988: Numerical simulation of tropical cumulus clouds and their interaction with the subcloud layer. *J. Atmos. Sci.*, 45, 2221–2250, doi: 10.1175/1520-0469(1988)045,2221:NSOTCC.2.0.CO;2.

Larson, V. E., & Golaz, J.-C. (2005). Using probability density functions to derive consistent closure relationships among higher-order moments. *Monthly Weather Review*, 133(4), 1023–1042.

Lareau, Neil P. "Subcloud and Cloud-Base Latent Heat Fluxes during Shallow Cumulus Convection". *Journal of the Atmospheric Sciences* 77.3 (2020): 1081-1100. <https://doi.org/10.1175/JAS-D-19-0122.1>.

Larson, Vincent E., Jean-Christophe Golaz, and William R. Cotton. "Small-Scale and Mesoscale Variability in Cloudy Boundary Layers: Joint Probability Density Functions". *Journal of the Atmospheric Sciences* 59.24 (2002a): 3519-3539. [https://doi.org/10.1175/1520-0469\(2002\)059<3519:SSAMVI>2.0.CO;2](https://doi.org/10.1175/1520-0469(2002)059<3519:SSAMVI>2.0.CO;2).

Larson, V. E., Golaz, J.-C., & Cotton, W. R. (2002b). Small-Scale and Mesoscale Variability in Cloudy Boundary Layers: Joint Probability Density Functions. *Journal of the Atmospheric Sciences*, 59(24), 3519–3539. [https://doi.org/10.1175/1520-0469\(2002\)059<3519:SSAMVI>2.0.CO;2](https://doi.org/10.1175/1520-0469(2002)059<3519:SSAMVI>2.0.CO;2)

Lemone, Margaret a. and William T. Pennell. "The Relationship of Trade Wind Cumulus Distribution to Subcloud Layer Fluxes and Structure." *Monthly Weather Review* 104 (1976): 524-539.

Lenschow, D. H., Mann, J., & Kristensen, L. (1994). How long is long enough when measuring fluxes and other turbulence statistics? *Journal Of Atmospheric And Oceanic Technology*, 11, 661-673. doi:10.1175/1520-0426(1994)011<0661:HLILEW>2.0.CO;2.

Moran, K., Pezoa, S., Fairall, C. W., Williams, C., Ayers, T., Brewer, A., de Szoeke, S. P., and Ghate, V.: A Motion-Stabilized W-Band Radar for Shipboard Observations of Marine Boundary-Layer Clouds, *Bound.-Lay. Meteorol.*, 143, 3–24, <https://doi.org/10.1007/s10546-011-9674-5>, 2012.

Morrison, H., & Gettelman, A. (2008). A New Two-Moment Bulk Stratiform Cloud Microphysics Scheme in the Community Atmosphere Model, Version 3 (CAM3). Part I: Description and Numerical Tests. *Journal of Climate*, 21(15), 3642–3659. <https://doi.org/10.1175/2008JCLI2105.1>

Medeiros B, Stevens B, Held I, Zhao M, Williamson DL, Olson J, Bretherton C (2008) Aqua planets, climate sensitivity, and low clouds. *J Clim* 21:4974–4991

Nusbaumer, J., Wong, T. E., Bardeen, C., & Noone, D. (2017). Evaluating hydrological processes in the Community Atmosphere Model Version 5 (CAM5) using stable isotope ratios of water. *Journal of Advances in Modeling Earth Systems*, 9(2), 949–977. <https://doi.org/10.1002/2016MS000839>

Pennell, W. T., and M. A. LeMone. "An Experimental Study of Turbulence Structure in the Fair-Weather Trade Wind Boundary Layer". *Journal of Atmospheric Sciences* 31.5 (1974): 1308-1323. < [https://doi.org/10.1175/1520-0469\(1974\)031<1308:AESOTS>2.0.CO;2](https://doi.org/10.1175/1520-0469(1974)031<1308:AESOTS>2.0.CO;2)>. Web. 3 Sep. 2022.

Pincus, R., Fairall, C. W., Bailey, A., Chen, H., Chuang, P. Y., de Boer, G., Feingold, G., Henze, D., Kalen, Q. T., Kazil, J., Leandro, M., Lundry, A., Moran, K., Naeher, D. A., Noone, D., Patel, A. J., Pezoa, S., PopStefanija, I., Thompson, E. J., Warnecke, J., and Zuidema, P.: Observations from the NOAA P-3 aircraft during ATOMIC, *Earth Syst. Sci. Data*, 13, 3281–3296, <https://doi.org/10.5194/essd-13-3281-2021>, 2021.

Pond, S., G. T. Phelps, J. E. Paquin, G. McBean, and R. W. Stewart. "Measurements of the Turbulent Fluxes of Momentum, Moisture and Sensible Heat over the Ocean". *Journal of Atmospheric Sciences* 28.6 (1971): 901-917. < [https://doi.org/10.1175/1520-0469\(1971\)028<0901:MOTTFO>2.0.CO;2](https://doi.org/10.1175/1520-0469(1971)028<0901:MOTTFO>2.0.CO;2)>.

Redelsperger, J. L. and G. Sommeria, 1986: Three-dimensional simulation of a convective storm: Sensitivity studies on subgrid parameterization and spatial resolution. *J. Atmos. Sci.*, 43, 2619–2635, doi: 10.1175/1520-0469(1986)043,2619:TDSOAC.2.0.CO;2.

Seifert A, Heus T (2013) Large-eddy simulation of organized precipitating trade wind cumulus clouds. *Atmos Chem Phys* 13(11):5631–5645. doi:10.5194/acp-13-5631-2013

Sherwood SC, Bony S, Dufresne JL (2014) Spread in model climate sensitivity traced to atmospheric convective mixing. *Nature* 505:37–42. doi:10.1038/nature12829

Schmeissner, T., R. A. Shaw, J. Ditas, F. Stratmann, M. Wendisch, and H. Siebert. "Turbulent Mixing in Shallow Trade Wind Cumuli: Dependence on Cloud Life Cycle". *Journal of the Atmospheric Sciences* 72.4 (2015): 1447-1465. < <https://doi.org/10.1175/JAS-D-14-0230.1>>.

Sørensen, L.L., Larsen, S.E. Atmosphere–Surface Fluxes of CO<sub>2</sub> using Spectral Techniques. *Boundary-Layer Meteorol* 136, 59–81 (2010). <https://doi.org/10.1007/s10546-010-9499-7>

Starr Malkus, Joanne. "SOME RESULTS OF A TRADE-CUMULUS CLOUD INVESTIGATION". *Journal of Atmospheric Sciences* 11.3 (1954): 220-237. < [https://doi.org/10.1175/1520-0469\(1954\)011<0220:SROATC>2.0.CO;2](https://doi.org/10.1175/1520-0469(1954)011<0220:SROATC>2.0.CO;2)>.

Stevens, B., Bony, S., Farrell, D., Ament, F., Blyth, A., Fairall, C., ...: EUREC<sup>4</sup>A, Earth Syst. Sci. Data, 13, 4067–4119, <https://doi.org/10.5194/essd-13-4067-2021>, 2021.

Thompson, N. et al. “Eddy-fluxes and spectra in the GATE sub-cloud layer.” Quarterly Journal of the Royal Meteorological Society 106 (1980): 277-292.

Vial J, Dufresne JL, Bony S (2013) On the interpretation of inter-model spread in cmip5 climate sensitivity estimates. Clim Dyn 41(11):3339–3362. doi:10.1007/s00382-013-1725-9

Vial J, Bony S, Stevens B, Vogel R (2017) Mechanisms and model diversity of trade-wind shallow cumulus cloud feedbacks : a review. Surv Geophys. doi:10.1007/s10712-017-9418-2

Vogel R, Nuijens L, Stevens B (2016) The role of precipitation and spatial organization in the response of trade-wind clouds to warming. J Adv Model Earth Syst 8(2):843–862. doi:10.1002/2015MS000568

Webb M, Senior C, Sexton D, Ingram W, Williams K, Ringer M, McAvaney B, Colman R, Soden B, Gudgel R et al (2006) On the contribution of local feedback mechanisms to the range of climate sensitivity in two GCM ensembles. Clim Dyn 27(1):17–38

Zhang, G. J., & McFarlane, N. A. (1995). Sensitivity of climate simulations to the parameterization of cumulus convection in the Canadian climate centre general circulation model. Atmosphere-Ocean, 33(3), 407–446. <https://doi.org/10.1080/07055900.1995.9649539>